Does albedo control predominantly the Seasonal South Polar Cap recession ?

Frédéric Schmidt [a], Sylvain Douté [a], Bernard Schmitt [a], Jean-Pierre Bibring [b], Yves Lanvevin [b], and the OMEGA Team

[a] *Laboratoire de Planétologie de Grenoble, Université de Grenoble, CNRS, INSU, BP 53, 38041 Grenoble Cedex 9, France*

[b] *Institut d'Astrophysique Spatiale, Université Paris XI, Bâtiment 121, 91405 Orsay cedex, France*

Number of pages: **??**
Number of tables: 6
Number of figures: 10

Email address: `fschmidt@obs.ujf-grenoble.fr` (Frédéric Schmidt).

Proposed Running Head:
Albedo control SSPC recession

Please send Editorial Correspondence to:

Frédéric Schmidt
Laboratoire de Planétologie de Grenoble, Université de Grenoble
BP 53
38041 GRENOBLE CEDEX 9
FRANCE

Email: fschmidt@obs.ujf-grenoble.fr
Phone: +33 4.76.51.41.54
Fax: +33 4.76.51.41.46

ABSTRACT

Since several decades, GCM simulates current time martian climate. The calibration of those GCMs at present time is a crucial step to understand the climate history of Mars. One of the major climatic signal that validates current GCMs is the annual pressure cycle.

Evolution of the surface covered by the seasonal deposit has been difficult to use to calibrate the GCMs due to spectral ambiguities between CO_2 and H_2O ice in the visible range. Now, in particular with the imaging spectrometer OMEGA in the near infra-red range, it is possible to follow both ices at a spatial resolution of about 1 km. At global scale, we determine the time evolution of the Seasonal South Polar Cap (SSPC) crocus line, defining the edge of the SSPC. This crocus line is not symmetric around the geographic South pole. At local scale, we introduce the snowdrop distance, describing the local structure of the SSPC edge. Both crocus line and snowdrop distance should now be used to calibrate GCMs.

Albedo of the seasonal deposits is usually an uniform and constant parameter of the GCMs. In the light of this study, albedo is the main parameter that controls the SSPC recession at both global and local scale. Using a defrost mass balance model, that incorporates the effect of shadow induced by topography, we show that the SSPC asymmetry in the crocus line is controlled by albedo. At local scale, we show that the snowdrop distance is correlated with the albedo variability. Further GCM improvements should integrate these two points. The next attempt is to identify and model the process(es) in the origin of those albedo differences.

Keywords: MARS, SURFACE, MARS, POLAR CAPS, ICES, SPECTROSCOPY

1 Introduction

A fraction of the Martian atmosphere, which is mainly composed of CO_2, is trapped during winter at the surface at high latitude in the form of CO_2 frost. When the Sun light returns in spring, this frost is heated up, sublimates and CO_2 returns back to the atmosphere. This major martian climatic cycle has been revealed be the pioneer work of Leighton and Murray, 1966.
The imaging spectrometer OMEGA revealed that the Seasonal South Polar Cap (SSPC) of Mars, during its recession phase, is essentially composed of CO_2 ice. As discussed by Langevin et al., 2007, H_2O ice signature, in the solar longitude range Ls=110°-193°, is probably due to clouds in the atmosphere. Surface H_2O ice is present only at some specific locations over the range of Ls 220°-250°. At contrary, the Seasonal North Polar Cap involves both H_2O and CO_2 frost (Schmitt et al., 2006). In this article, we will only consider CO_2 in the SSPC.

During the recession phase, different processes of energy loss/gain are involved in the defrost mass balance : latent heat consumption due to CO_2 frost sublimation, thermal emission, absorption of direct and indirect (scattered) sunlight, absorption of thermal emission emitted by the atmosphere and the surrounding terrains, conduction of thermal energy in the ground. Different parameters are involved in those processes : albedo as suggested by Piqueux et al., 2003 and Colaprete et al., 2005, thermal emissivity as accurately modeled by Forget et al., 1998, slopes and surface roughness (Veverka and Goguen, 1973; Aharonson and Schorghofer, 2006), thermal inertia of the ground (Aharonson, 2004), annual surface pressure change, altitude, heat advection from the atmosphere.

Recent Global Climate Models (GCM), integrating processes involved in the CO_2 cycle (including CO_2 snow formation and precipitation), are able to reproduce the Viking Lander 1 pressure measurements (Forget et al., 1998, 1999), assuming an uniform and constant albedo value for the seasonal caps and no surface slope effects. Nevertheless, albedos observed by Viking (James et al., 1979), more recently by TES (Kieffer et al., 2000) and by OMEGA (Langevin et al., 2007) are changing in space and time.
Current GCMs are able to reproduce the time evolution of the surface area covered by CO_2 frost (Lewis et al., 1999). In order to enhance our confidence in both present and past climate studies, the next generation of GCMs should reproduce the latitude of the so called "crocus line" at local scale as a function of longitude and time. For that purpose they must take into account the time and space evolutions of the parameters controlling the processes listed above.

The aim of this article is to determine the relative importance of these factors in the control of the SSPC recession.

We will pursue the following objectives :

(1) Following the spatial distribution and albedo of H_2O and CO_2 ices in the SSPC as a function of time using a set of OMEGA observations for the time period ranging from Ls=110° to Ls=320°. For that purpose we notably use an automatic detection algorithm. Concepts describing the structure of the SSPC edge ("inner crocus line", "outer crocus line" and "snowdrop time") are introduced based on detection statistics inside latitudinal bins. The evolution of the latitude and structure of the SSPC edge as a function of time and longitude constitutes our main constraint. (Section 2).
(2) Modeling, for an ice layer, the daily and cumulative CO_2 frost mass budget by integrating the radiative gains and losses from or toward space as well as the conductive heat coming from the ground. A special care will be done in the modeling of the topography induced shadow. The mass balance is calculated for individual facets with their own altitude and slope orientation based on MOLA DTM. (Section 3)
(3) Performing a sensitivity study of the model regarding to its principal parameters : thermal inertia of the ground linked with subsurface heat release, altitude linked with the temperature of the CO_2 layer, surface roughness linked with shadowing effects and thus with absorption of solar light, emissivity linked with thermal emission of the ice (section 4).
(4) Challenge the model with various measurements of the SSPC : accumulation retrieved from neutron flux measurements by GRS and HEND, spatial and temporal distribution of the CO_2 ice occurrence as determined by OMEGA (see objective 1.), spatial and temporal distribution of the CO_2 ice albedo as measured by OMEGA (see objective 1.). This analysis is done at two spatial scales :
    (a) global scale (i.e. : flat south polar region divided into two longitude sectors : cryptic and anti-cryptic) : we show that the model is compatible with all measurements, using simple analytical laws for the visible and infrared albedo dependence with latitude and time (section 4.1.8).
    (b) local scale (i.e. : rough south polar region, divided into facets at a resolution of 1 km) : we demonstrate that the structure of the SSPC edge cannot be predicted by the model using the smooth albedo variation already used at global scale. We found a correlation between the structure of the SSPC edge and the distribution of albedo observed by OMEGA (section 4.2).
(5) Discussion of the processes that potentially govern the albedo global asymmetry between the cryptic and anti-cryptic sectors and that can explain the albedo variability at lower spatial scale. (Section 5).

2 Analyzing a sequence of OMEGA/MEX observations for monitoring CO_2 and H_2O ices

2.1 Selection of OMEGA observations

The imaging spectrometer OMEGA on board Mars Express has acquired the most comprehensive set of observations to date in the near-infrared (0.93-5.1 microns) on the SSPC from winter solstice to the end of the recession at Ls=325° (Langevin et al., 2007). Monitoring the spatial distribution of CO_2 and H_2O ices requires their automatic detection due to the large number of images. For that purpose we use a method called "Wavanglet", that we developed especially (Schmidt et al., 2007) and that is described shortly in the next section.

From Ls=110° to Ls =320° of martian year 27 (early 2005 to mid 2006) we select a total of 605 OMEGA/MEX observations with a positive detection of CO_2 ice at high southern latitudes.

2.2 Wavanglet detection method

The detection is carried on by comparing each spectrum of an image with reference spectra of compounds we want to detect in an optimized subspace of wavelets. The correlation between the reduced observed and reference spectra is calculated and compared to a threshold in order to declare detection (1) or absence (0). After the processing of an OMEGA image, the Wavanglet algorithm provides one binary image with the same spatial dimensions - called *detection mask* - for each reference compounds (Schmidt et al., 2007).

We take into account the information about corrupted spectels and lines and we systematically remove spectra acquired with incidence angles higher than 85° and/or emergence angles higher than 70° (low signal to noise ratio). In this study we use four references : one synthetic (i.e. generated by a radiative transfer model) spectrum of CO_2 ice, one synthetic spectrum of H_2O ice, one endmember spectrum of dust extracted from an OMEGA image, and one endmember spectrum of water ice clouds observed over Hellas.

2.3 Position and structure of the polar cap edge

Previous studies about the south seasonal cap recession were conducted by Kieffer et al. (2000) using the TES instrument. These authors consider that

a sudden rise of surface temperature, from around 145K - the temperature of CO_2 ice in equilibrium with the atmosphere - to about 230K - the temperature of the mineral bare ground - indicates the passage of the sublimation front. For a given location, fitting the temporal evolution of the temperature by an arctangent empirical law provides the crocus date which, by definition, coincides with the inflection of the curve. The crocus line is the set of locations, where the crocus dates are equal to a given Ls. In the visible range, another specific law is used to parametrize the decrease of albedo and evaluate the crocus date, assuming such event coincides with CO_2 disappearance. These studies already suggested that the edge of the seasonal cap is a transition zone where patches of CO_2 ice and dust coexist geographically over a certain spatial extent.

In this article, we propose to characterize the transition zone by defining "inner and outer crocus lines" from CO_2 detection by OMEGA in the near infrared. Let introduce a *bin,* an element 0.3° and 10° wide respectively in latitude and longitude belonging to a geographical grid. Hundreds of OMEGA pixels usually fall into such a bin allowing to calculate statistics for different physical quantities. A *meridian profile* is the latitude sequence of values calculated for the bins falling in the same longitude range (see appendix A).

First we segment all CO_2 detection mask (see previous section) into bins. The OMEGA spatial resolution can change from 2 km to 700 m depending on observation conditions but the bin size is kept constant. The same grid is used to represent the model results (appendix A for definition of scales). For each bin, the CO_2 *ice coverage* indicator f_{CO_2} is the number of pixels with positive detection of CO_2 divided by the total number of pixels. Should some sub-pixel mixing occurs, a positive detection for a pixel does not mean that the latter is entirely covered by frost. As a consequence f_{CO_2} is the upper limit of the real coverage of the bin by CO_2.

Second, we build a meridian profile of CO_2 ice coverage for each individual OMEGA image corresponding to a given Ls. The bins that contain a border (border of the observation, border of corrupted portions of an image) are eliminated in order to prevent biases.

Third, from each meridian profile, we extract the inner/outer limits of the SSPC by following 3 rules :

- outer crocus line: the bin that contains a CO_2 ice coverage f_{CO_2} higher than 1% and that is the closest to the equator.
- inner crocus line: the bin that contains a CO_2 ice coverage f_{CO_2} lower than 99% and that is the closest to the pole.
- Inner and outer crocus line: the bin that contains the inner/outer crocus line is valid only if its adjacent neighbor bins contain no image border.

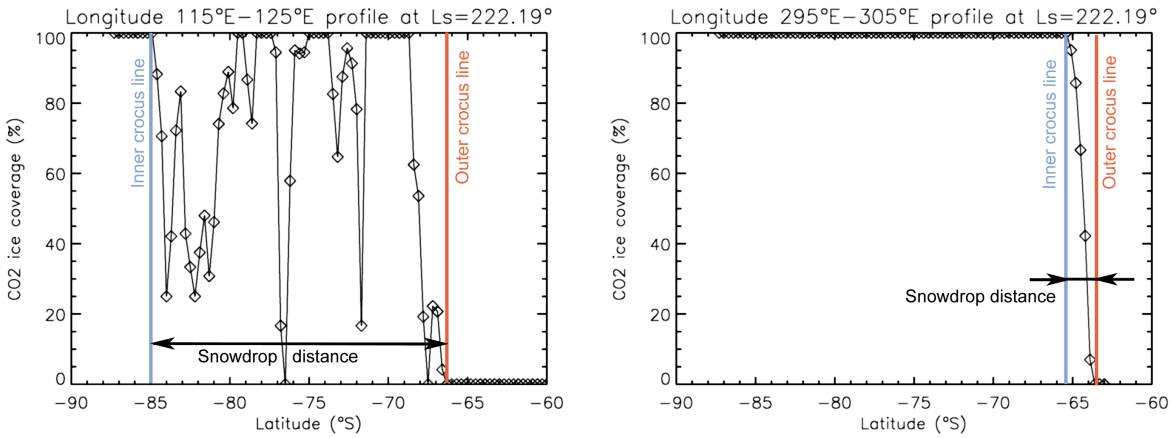

(a) Cryptic sector (b) Anticryptic sector

Figure 1. Structure of the SSPC edge. Definition of the snowdrop distance at Ls=222.19° for two extreme cases : (a) meridian profile in the cryptic sector (longitude range 115°E-125°E) where the transition zone of CO_2 ice coverage is wide and chaotic. (b) meridian profile in the anti-cryptic sector (longitude range 195°E-305°E) where the transition zone of CO_2 ice coverage is regular and narrow.

By treating our selection of OMEGA images, we sample the latitude as a function of time for both crocus lines at discrete values of Ls for 36 intervals of 10° longitude. At a given location, following the definition by Kieffer et al., 2000, we propose to name the date when the inner crocus line - respectively outer crocus line - crosses that location : the "inner crocus date" - respectively "outer crocus date".

The latitudinal distance (resp. temporal gap) between the inner and outer crocus lines (resp. crocus date) that defines the width (resp. time) of the CO_2 snow drop, can be named : SNOW-DROP. Accidentally, the term "snowdrop" denotes also a flower that grows through the spring snow on the Earth. For the convenience, as we favor gorgeous flowers over inelegant acronyms, we propose to use simply "snowdrop".

At global scale, the position of the SSPC observed by OMEGA, described by the mean crocus line, is usually not symmetric around the geographic south pole. At local scale, the structure of the SSPC edge, described by the snowdrop time, changes with time/latitude and longitude. One goal of this paper is to understand these patterns and relate them to processes and physical parameters.

2.4 Monitoring the albedo with OMEGA

Calculating the instantaneous or integrated CO_2 mass budget requires the monitoring of its bolometric albedo. Definition of this spectrally integrated, directional-hemispheric albedo can be found in Hapke, 1993. Practically its accurate evaluation requires multi-angular sampling either consecutive (Paige and Ingersoll, 1985) or simultaneous (for instance with CRISM instrument by Murchie et al., 2004) of the bidirectional reflectance distribution function (BRDF) of the icy terrains. Multi-angular OMEGA data (EPF) that would allow us to constrain the BRDF prior to directional integration are very sparse in space and time. As a consequence monitoring the bolometric albedo of the whole SSPC from OMEGA images is out of the scope of this paper. As a crude approximation we will use instead the reflectance $R^O_{1.07}$ measured by OMEGA in the continuum at 1.07 microns for a combination of incidence and emergence angles that vary weakly from pixel to pixel.

$$A_{dh,vis}\left(\theta_i\right) = A_{vis} \simeq R^O_{1.07}\left(\theta_i, \theta_e, \theta_a\right) \tag{1}$$

with θ_i the incidence angle, θ_e the emergence angle, and θ_a the azimuth.

This channel was also proposed by Langevin et al., 2007 who argues that it combines high signal to noise ratio, high radiometric accuracy and no absorption bands due to CO_2 ice, H_2O ice and CO_2 gas. Nevertheless aerosols in the atmosphere can affect the reflectance at 1.07 microns and thus could introduce a bias in our estimation. We can note that, after Ls=220°, water ice clouds are completely absent of the south polar region.

In this study, we calculate the average and the variance of the "albedo" in each bin of the grid based on the pixels with positive detection of CO_2 (see Appendix A for definition of scales). Such quantity will be denoted A^O_{vis}.

3 Modeling the daily and cumulative CO_2 frost mass budget

3.1 Topography and roughness measured by MOLA

The MOLA topographic dataset covers the south polar region at a resolution 1/64 degree (available on line [1]). The dataset is interpolated where no data are recorded, especially near the geographic south pole from latitude 90°S to 86°S. We use a map built according to a south polar stereographic projection and a

[1] http://pds-geosciences.wustl.edu/missions/mgs/megdr.html

resolution of 920 m, comparable to the best OMEGA spatial resolution (≈700 m). Better spatial resolution is available but, in this case, the calculation time of our model would be too long (in excess of one month). We assimilate each pixel of the MOLA dataset to a facet. (See Appendix A for definition of scales).

3.1.0.1 MOLA topography We calculate the local slope of a facet in terms of the geographic coordinates by differentiating the MOLA topography $h(x, y)$, using the following operator :

$$\begin{cases} \frac{\partial}{\partial L} = \frac{2R\cos(\phi)}{1-\sin(\phi)} \left(-\sin(L)\frac{\partial}{\partial y} + \cos(L)\frac{\partial}{\partial x} \right) \\ \frac{\partial}{\partial \phi} = \frac{2R}{1-\sin(\phi)} \left(\cos(L)\frac{\partial}{\partial y} + \sin(L)\frac{\partial}{\partial x} \right) \end{cases} \quad (2)$$

L being the longitude, ϕ the latitude, R the radius of the planet and (x, y) the map coordinates. The derivatives are estimated by $\frac{\partial}{\partial x}h(x_i, y_i) = \frac{h(x_{i+1},y_i)-h(x_i,y_i)}{x_{i+1}-x_i}$.

This method has the advantage to produce a result for all points in this projection. Nevertheless, the errors due to the map projection, and to the interpolation of several MOLA points are difficult to estimate.

3.1.0.2 MOLA roughness Surface roughness is defined relatively to all scales higher than the facet size. Several statistical descriptors of this quantity can be found in the literature (Shepard et al., 2001; Aharonson et al., 2001) : standard deviation of the altitude $h(x, y)$ from the mean or more robustly from the median, interquartils, decorrelation length. Pioneer work about roughness as an instance of fractal distribution was done by Sayles and Thomas, 1978. Such description was applied for the north polar cap using MOLA data by Malamud and Turcotte, 2001. They used wavelets to estimate roughness as the local value of the power law dependence of the power spectral density on frequency. They estimates $\beta \simeq 3.5$ for the South permanent cap and $\beta \simeq 2$ for the surrounding terrains. An alternative theory describes roughness as the local value of the exponent of the RMS slope as a function of baseline, i.e. the Hurst exponent H. Recently Aharonson and Schorghofer, 2006 estimated a local value of H which is about 0.8 for both global Mars and the region occupied by the seasonal south polar cap. In this study, we use the Hurst exponent fractal description of the roughness because an adapted model of self shadowing function is provided by Shepard and Campbell, 1998.

The study by Campbell et al., 2003 suggests that the MOLA dataset cannot be extrapolated for roughness scales lower than 15 m. In addition, no dataset are available for the complete south polar region of Mars. In this article, the roughness at scales below the facet size are ignored.

3.2 Daily averaged radiation absorbed by frost

3.2.1 Estimation of the different contributions

Computing the seasonal radiation budget is an important step to understand the climate of the polar regions. From the parametrization of the "instantaneous" absorbed energy Q made by Kieffer et al., 1977; Schorghofer and Aharonson, 2005; Aharonson and Schorghofer, 2006, we will compute the daily averaged absorbed radiation W at a given location of the surface of Mars using the integration method used by (Laskar et al., 1993). There are four sources : the direct sunlight Q_{sun}, the sunlight scattered by the atmosphere Q_{scat}, the thermal emission by the atmosphere Q_{IR} and the thermal emission by the neighboring facets Q_{floor}.

$$W = \int (Q_{sun} + Q_{scat} + Q_{IR} + Q_{floor})\, dt \tag{3}$$

All these terms depend on local slope γ. We will use the following notation for three normalized vectors : $\overrightarrow{r_{surf}}(L, \phi)$ the radius vector of a point at the surface assuming a spherical planet, $\overrightarrow{r_{sun}}(\alpha, \delta)$ the radius vector of the subsolar point, and $\overrightarrow{n_{surf}}(L_n, \phi_n)$ the direction normal to the local surface. The coordinate are expressed in East increasing longitude (L, α, L_n are from 0 to 2π) and latitude (ϕ, δ, ϕ_n are from $-\frac{\pi}{2}$ to $\frac{\pi}{2}$). The local slope γ is defined as :

$$\gamma = \arctan \sqrt{\left(\frac{\partial topo}{\partial \phi}\right)^2 + \left(\frac{\partial topo}{\partial L}\right)^2} \tag{4}$$

In order to simplify the equation, the integration of the "instantaneous" insolation is performed relative to longitude L instead of time Laskar et al. (1993), assuming that the relative orientation of the planet rotation axis and the sun direction is constant during a day, which is a reasonable assumption for planet Mars. The integration method is described in appendix B.

Integration of the different contributions Q_{sun}, Q_{scat}, Q_{IR} and Q_{floor} are explicitly described below :

(1) Direct sun illumination

$$Q_{sun} = \frac{S_{sun}}{r_{sun}^2}(1 - A_{vis})(1 - f)^{1/\max((\overrightarrow{r_{surf}} \bullet \overrightarrow{r_{sun}}), 0.04)}(\overrightarrow{n_{surf}} \bullet \overrightarrow{r_{sun}})\Psi(\overrightarrow{r_{surf}} \bullet \overrightarrow{r_{sun}}, H, \gamma) \tag{5}$$

The first ratio is the solar constant at the heliocentric distance of Mars, the second factor expresses the absorption of radiation by the surface, the third represents the parametrized atmospheric attenuation (Kieffer et al.,

1977; Schorghofer and Aharonson, 2005; Aharonson and Schorghofer, 2006), the fourth term express the geometrical effect and the fifth term Ψ quantifies the loss of illumination due to self-shadowing effects linked with roughness. In the following, these five factors will be noted F_1 to F_5. We use the empirical shadowing function for fractal surface $\Psi(\overrightarrow{r_{surf}} \bullet \overrightarrow{r_{sun}}, H, \gamma)$, truncated to the 6th term, determined by Shepard and Campbell, 1998 :

$$\Psi(\overrightarrow{r_{surf}} \bullet \overrightarrow{r_{sun}}, H, \gamma) = 1 - \frac{1}{2}\sum_{n=1}^{6} \frac{1}{2.3^{n-1}} erfc\left(\frac{n^{1-H}}{\sqrt{2}\frac{\sqrt{1-\left(\overrightarrow{r_{surf}} \bullet \overrightarrow{r_{sun}}\right)^2}}{\left(\overrightarrow{r_{surf}} \bullet \overrightarrow{r_{sun}}\right)} \tan(\gamma)}\right) \quad (6)$$

Using equations 2, 3, 5 and 6, we can see that Q_{sun} depends on L only through the scalar products :

$$Q_{sun} = F_1.F_2.F_3\left(\cos(L-\alpha)\right).F_4\left(\cos(L-\alpha+L'+L_c)\right).F_5\left(\cos(L-\alpha)\right) \quad (7)$$

$$W_{sun} = \frac{1}{2\pi}\int_{\alpha+C}^{\alpha+D} Q_{sun}(L)dL = \frac{1}{2\pi}\int_{C}^{D} \tilde{Q}_{sun}(\tilde{L})d\tilde{L} \quad (8)$$

with $\tilde{L} = L - \alpha$, $C = -H_{n0} - L' - L_c$, $D = H_{n0} - L' - L_c$ and $\tilde{Q}_{sun} = F_1.F_2.F_3\left(\cos(\tilde{L})\right).F_4\left(\cos(\tilde{L}+L'+L_c)\right).F_5\left(\cos(\tilde{L})\right)$.
This shows that W_{sun} is independent on α, the longitude of the sub-solar point. We set this parameter to zero and estimate the integral 8 using a Simpson's numerical integration scheme (Press et al., 1986-1992).

(2) Indirect solar illumination through scattering in the atmosphere and absorbed by the surface following Kieffer et al., 1977 and Aharonson and Schorghofer, 2006 :

$$Q_{scat} = \frac{S_{sun}}{r_{sun}^2}(1-A_{vis})\frac{1}{2}f_{scat}\cos^2(\frac{\gamma}{2}) \quad (9)$$

$$W_{scat} = \frac{1}{2\pi}\int_{0}^{2\pi} Q_{scat}dL = Q_{scat} \quad (10)$$

$$W_{scat} = \frac{1}{2\pi}\int_{0}^{2\pi} Q_{scat}\Pi_{L_{min}}^{L_{max}}dL = \frac{H_{n0}}{\pi}Q_{scat} \quad (11)$$

(3) Surface heating by thermal emission of the atmosphere following Kieffer et al., 1977 and Aharonson and Schorghofer, 2006 :

$$Q_{IR} = \frac{S_{sun}}{r_{sun}^2}(1-A_{IR})f_{IR}\cos^2(\frac{\gamma}{2})\left(\overrightarrow{r_{surf}} \bullet \overrightarrow{r_{sun}}\right)_{noon} \quad (12)$$

The cosine of the incidence angle at noon for a flat surface : $(\overrightarrow{r_{surf}} \bullet \overrightarrow{r_{sun}})_{noon}$

$$(\overrightarrow{r_{surf}} \bullet \overrightarrow{r_{sun}})_{noon} = (\overrightarrow{r_{surf}} \bullet \overrightarrow{r_{sun}})_{L=\alpha} = \sin(\frac{\pi}{2} + \phi - \delta) \tag{13}$$

$$W_{IR} = \frac{1}{2\pi} \int_0^{2\pi} Q_{IR} dL = Q_{IR} \tag{14}$$

(4) Surface heating by thermal emission of the surrounding soil, as in Kieffer et al., 1977 and Aharonson and Schorghofer, 2006:

$$Q_{floor} = \varepsilon \sigma T^4 (1 - A_{IR}) \sin^2(\frac{\gamma}{2}) \tag{15}$$

$$W_{floor} = \frac{1}{2\pi} \int_0^{2\pi} Q_{floor} dL = Q_{floor} \tag{16}$$

The parameters values used for the surface radiation budget are summarized in appendix C.

3.3 Daily and cumulative defrost mass balance

3.3.1 Estimation of the "instantaneous" CO_2 defrost balance

We estimate the instantaneous CO_2 frost mass balance using the energy balance at the surface. We compute the daily radiation budget and neglect the heat advection from the atmosphere, which is a correct hypothesis for the sublimation phase as suggested by GCM studies (Forget, 1998). The flux of mass resulting from the energy balance is :

$$\frac{\partial M_{CO_2}}{\partial t} = (F^{out}_{therm} - W^{in}_{sun} - W^{in}_{scat} - W^{in}_{IR} - W^{in}_{floor} - F^{in}_{cond}) \frac{1}{L_{CO_2}} \tag{17}$$

This equation can also be used for the daily balance assuming that the albedo and surface temperature of the facet do not change within the course of a day. A possible recondensation of CO_2 during the night on bare ground during the SSPC recession is not taken into account in this modeling. We neglect heat diffusion within the frost deposits by absorption and release of latent heat due to sublimation/recondensation and gas diffusion. We assume no metamorphism.

The different contributions of equation 17 are described below :

(1) Energy loss : outgoing thermal flux from CO_2 frost at the surface. This term is estimated by a gray body emission as proposed by Warren et al.,

1990 :

$$F_{therm}^{out} = \varepsilon\sigma T_{surf}^4 \tag{18}$$

Surface temperature T_{surf} is determined assuming that CO_2 frost at the surface is in equilibrium with atmospheric CO_2 gas at surface pressure P_{surf}. We use the surface pressure calculated by the GCM of Forget et al., 1999 for a given date (season) and location. This estimation takes into account the annual pressure cycle measured by Viking.
We use the empirical parametrized saturation curve proposed by Brown and Ziegler, 1979 to convert P_{surf} into temperature T_{surf}. This method is only correct when CO_2 frost is already present on the facet.

(2) Energy gain : absorbed radiative flux :

$$-W_{sun}^{in} - W_{scat}^{in} - W_{IR}^{in} - W_{floor}^{in} \tag{19}$$

Those terms are estimated according to the method described in the section 3.2 (equation 3).

(3) Energy gain : conducted internal heat flux from planet Mars. It has two different origins :
   (a) Annual heat wave in the ground. This term can be neglected during the recession phase, as demonstrated in section 4.1.3.
   (b) Geothermal heat flux. There is no direct measurement of the heat flux from planet Mars but several authors estimated that it is between 15 and 45 $\mathrm{mW.m^{-2}}$ on the average (Shchuko et al., 2003). For comparison, on Earth the average value is around 80 $\mathrm{mW.m^{-2}}$. We assume that it is spatially and temporally constant :

$$F_{cond}^{in} = 40\,\mathrm{mW.m^{-2}} \tag{20}$$

The order of magnitude of this flux is generally negligible in the cumulative frost balance when compared with the other terms. Nevertheless, for facets in the shadow, it could accelerate the occurrence of the crocus date.

3.3.2 Cumulative mass loss during recession

We can estimate the cumulative mass loss of frost during the SSPC recession by integrating the "instantaneous" frost mass balance. We perform the integration over Ls between 90° and 355° with a time step of 5°. We start the calculation when the balance becomes negative, at a date noted T_{beg}^M (beginning of the recession as determined by the model M), that is when the seasonal polar cap begins to sublimate. The date T_{beg}^M depends mainly on latitude, albedo and slope. We note the crocus date, the date of the end of the sublimation, T_{end}^M.

To convert Julian time expressed in seconds into time expressed in °Ls , we use the J2000 relations that can be found in Allison and McEwen, 2000.

The parameters used for modeling the defrost mass balance are summarized in appendix D.

3.4 Latitudinal profiles of W and M_{CO_2}

We perform the calculation of the absorbed radiation W and of the frost mass balance M_{CO_2} for all the facets of the MOLA grid expressed in stereographic south projection. In order to compare both modeled and observed crocus lines, we arrange the facets inside the set of bins described in section 2.4. For each bin, we calculate the mean and the variance of W and M_{CO_2}, both based on the population of facets within the bin. We present the results in the form of meridian profiles (see section 2.3).

Both daily absorbed radiation and defrost mass are estimated every 5° of Ls (almost 10 martian days). This time sampling interval is a compromise between accuracy and computational time (1 month for the M_{CO_2} on a bi-processor AMD Opteron 250, 64 bits, 2.4 Ghz).

4 Results

At global scale, we show that the asymmetry of the SSPC crocus line is a consequence of a pre-existing asymmetry of the visible albedo. For both the cryptic and anti-cryptic sectors, we find that our sublimation model is compatible with the net accumulation measurements by HEND and GRS, as well as with the crocus line and albedo determined by OMEGA. At local scale, the SSPC snowdrop distance is controlled by the state of albedo distribution more than 5° of Ls before the crossing of the inner crocus line.

We perform a sensitivity study that demonstrates that during the recession phase the following effects/parameters have limited effects on CO_2 stability: heat exchange with the ground, altitude, surface roughness (slope and shadow), emissivity and albedo in the thermal infrared.

The accumulation field is difficult to estimate accurately because the only measurements come from instruments with a large footprint. In addition, no accurate modeling is currently available. We suppose for our calculations that the net accumulation has a smooth latitudinal dependency.

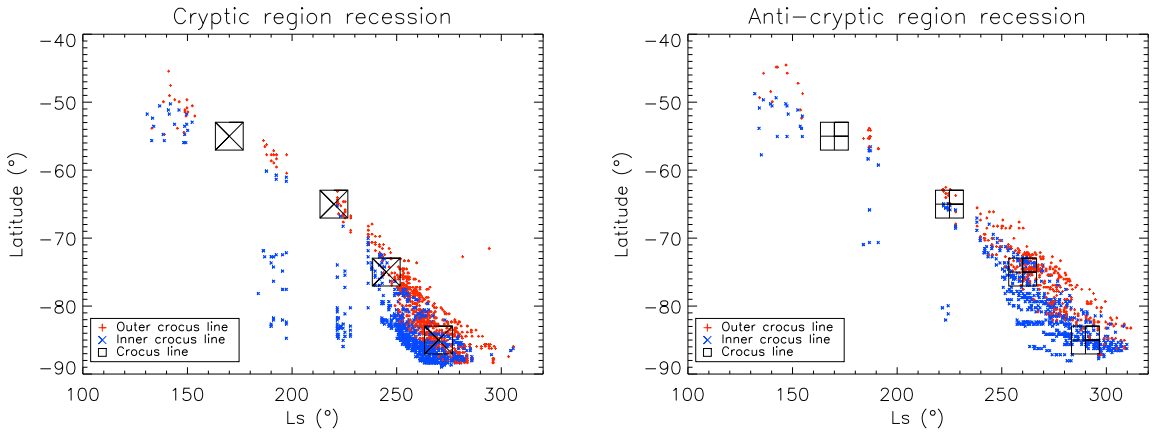

Figure 2. SSPC recession for both cryptic (between longitude 60°E and 260°E) and anti-cryptic sectors (between longitude 100°W and 60°E.). Small cross symbols represent the crocus lines points determined by our algorithm (see section 2.3). Large symbols represent the average position of the crocus line for four latitude.

4.1 Recession at global scale

The global SSPC recession is not symmetric around the geographic south pole as previously observed by Viking (James et al., 1979). Using TES data, Kieffer et al., 2000 define the *cryptic region* that recesses faster. This asymmetry is also observed with OMEGA data as mentioned by Langevin et al., 2007. We define the cryptic sector between longitude 60°E and 260°E, the anti-cryptic sector being the complementary, i.e. between longitude 100°W and 60°E.
In order to roughly describe the asymmetry, we estimate the OMEGA crocus line for both sector. We take the middle line between the inner and the outer crocus line (fig 1), to ensure coherence with the definition by Kieffer et al., 2000. The crocus date can be noted T^O_{end}, as the date of the end of the recession observed by OMEGA. We estimate the crocus date for 4 latitudes that are also considered in a HEND study by Litvak et al., 2007. At latitude 65°S, the typical crocus date is Ls=220° for the cryptic sector and Ls=225° for the anti-cryptic sector. At latitude 85°S, the difference goes up to 20°Ls.
In the cryptic sector, some seemingly defrosted points (outliers) are present at latitudes higher than 70°S in the time period from Ls=180° to Ls=230° (fig 2). This is due to the fact that some CO_2 deposits of the cryptic sector are covered by an optically thick mantle of dust as suggested by Langevin et al., 2006.

Now we discuss about the origin of the SSPC recession asymmetry that we illustrate by two representative meridian profiles : (a) within the cryptic sector (140°-150°E) and (b) within the anti-cryptic sector (270°-280E).
For that purpose we perform a sensitivity study of the defrost model, relative to the following effects/parameters on $\frac{\partial M_{CO_2}}{\partial t}$: annual heat wave in the ground,

altitude, surface roughness, albedo and emissivity in the IR and finally albedo in the visible. We also discuss the degree of spatial asymmetry of the accumulation $M_{CO_2/tot}$ and the date of the beginning of sublimation T_{beg} as well as of the previous parameters.

4.1.1 CO_2 *ice accumulation:* $M_{CO_2/tot}$

From a theoretical point of view, according to Forget, 1998, the mass balance during the net accumulation phase is governed by equation :

$$\frac{\partial M_{CO_2}}{\partial t} = (F^{out}_{therm} - F^{in}_{adv} - F^{in}_{cond} - W^{in}_{sun} - W^{in}_{scat} - W^{in}_{IR} - W^{in}_{floor})\frac{1}{L_{CO_2}} \quad (21)$$

The term F^{out}_{therm} represents the thermal flux (eq 18). It depends on emmissivity ε and altitude via the temperature. During the polar night ε is estimated by $1 - BD_{25}$ with TES measurements by Eluszkiewicz and Moncet, 2003. Before Ls=140°, at latitude 87°S, they estimate that emissivity is around 0.9 for the cryptic sector and 0.75 for the anti-cryptic sector, leading to a lower accumulation mass in the last sector. This difference in accumulation is in apparent contradiction with a longer recession time for the anti-cryptic sector. Section 4.1.4 shows that altitude can be considered as symmetric around the south pole.
Equation 21 is slightly different from equation 17 that expressed the defrost mass balance. The additional term F^{in}_{adv} represents the atmospheric advection contribution. Pollack et al., 1990 show that this term is no longer negligible because it can reach 30 W.m^{-2}. This can be asymmetric due to the topographic forcing of Hellas and Argyre (Colaprete et al., 2005).
Moreover the annual heat wave contribution F^{in}_{cond} becomes one of the dominant sources of energy (Aharonson, 2004). On average, for the average SSPC, this term was estimated by Paige and Ingersoll, 1985 to be up to 20-30 W.m^{-2}. An asymmetrical thermal inertia of the subsurface would lead to an asymmetrical accumulation. However thermal inertia observed by TES is symmetrical around the pole (Putzig et al., 2005).
All radiation terms W are negligible because the main accumulation phase occurs during the night time.

From an observational point of view, Viking, TES and OMEGA have observed that the SSPC is symmetric around the pole before Ls=220° at the end of the net accumulation phase (James et al., 1979; Kieffer et al., 2000; Langevin et al., 2007). Moreover a study by Aharonson et al., 2004 using MOLA data reveals that the amplitude of the semi-annual cycle of elevation of the deposits shows no clear asymmetry in the accumulation phase. The HEND (Litvak et al., 2007) and the GRS (Kelly et al., 2006) instruments have not enough spatial resolution to measure several meridian profile of accumulation according to

longitude.

We conclude that accumulation is likely symmetrical around the geographic south pole.

4.1.2 Date of the beginning of sublimation: T_{beg}

From a theoretical point of view, T_{beg} is the date when 21 is null. Thus the asymmetry of T_{beg} depends on the asymmetry of all terms. The first three terms was previously discussed in last section.
The radiation terms W are no more neg legible and will be discussed in sections 4.1.5 to 4.1.7. The most likely parameter that can be asymmetric is the albedo but the measurement by TES shows that albedo is symmetric from Ls=175 to Ls=200° (Piqueux et al., 2003).

The date T_{beg} is difficult to observe. The only direct measurement is by HEND (Litvak et al., 2007) and the GRS (Kelly et al., 2006) instruments have not enough spatial resolution to measure T_{beg} as a function of longitude. Indirect measurement of altitude using MOLA data shows (Aharonson et al., 2004) no clear asymmetry.

Following the same argumentation as in last section, we conclude that the date of the beginning of sublimation T_{beg} is likely symmetrical around the geographic south pole. In the next models, T_{beg}will be an free parameter, fixed by the model itself.

4.1.3 Annual heat wave in the ground

As suggested by Aharonson, 2004, the excess of heat absorbed by the ground during summer is partially released in winter. The amount of heat involved in this annual wave depends on thermal inertia of the subsurface. We use the LMD 1D model (model M1) developed by Forget et al., 1999, to estimate the amount of energy that comes from the ground during the recession phase. We consider the cryptic and anti-cryptic sectors at four latitude points : 55°S, 65°S, 75°S, 85°S. Following the study by Aharonson, 2004, the parameters of the bare soil are : albedo $A_{vis} = 0.29$, emissivity $\epsilon = 0.99$. In the visible, the albedo of the frost is set to the equivalent albedo in the time independent scenario, model M2 (see section 4.1.8). We compute the subsurface heat released during the net sublimation phase for two extreme thermal inertia : 20 J.m^{-2}.s$^{-1/2}$.K^{-1} and 1000 J.m^{-2}.s$^{-1/2}$.K^{-1}, compatible with the range of apparent thermal inertia estimated for the south polar region determined by Putzig et al., 2005. The integration is conducted from the $T^H_{beg}(L', \phi)$ date of the beginning of net sublimation as measured by HEND to $T^{M1}_{end}(L', \phi)$ the date of the total sublimation of the CO_2 ice layer by this model M1. We run the model over

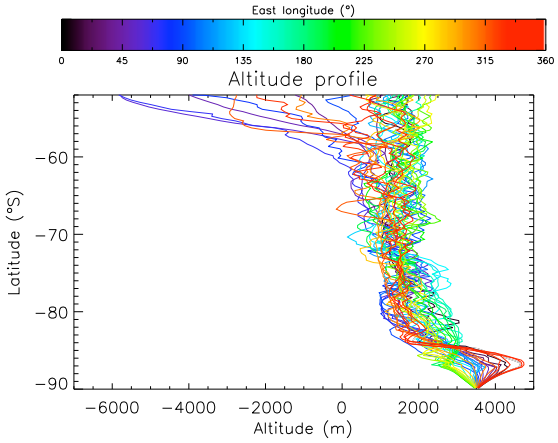

Figure 3. Topography of the SSPC region. Each color profile represents a mean meridian profile of the MOLA data. (see Appendix A)

Latitude (°S)	55	65	75	85
Altitude cryptic sector (m)	1000	1000	2000	2500
Altitude anti-cryptic sector (m)	1000	1000	2000	3500

Table 1
Reference altitude for both cryptic and anti-cryptic sectors.

three martian years to become insensitive to the initial conditions. Subsurface heat is converted to an equivalent sublimated CO_2 mass.
The results are displayed in table 4 for the cryptic sector and in table 5 for the anti cryptic sector. At maximum, 6% of the total mass sublimated is due to subsurface heat (at latitude 55°S) leading to a shift of the crocus date of less than 2°Ls. For comparison, the difference in crocus date between the cryptic and anti-cryptic sectors is about 20°Ls.

As a conclusion this source of energy can be neglected in all calculations concerning the recession phase. Nevertheless subsurface heat is one of the most important sources of energy during the polar night.

4.1.4 Altitude

Topography around the pole is quasi symmetric (fig 3). The maximum altitude difference between the anti-cryptic (orange-red profiles) and cryptic (blue-green profiles) sectors is ≈ 1000 m at latitudes higher than 84°S. Two particular regions depart from the general trend at latitudes lower that 60°S : Hellas basin (between 40°E and 90°E) with a minimum altitude of less than -6000 m and Argyre basin (between 300°E and 330°E) with a minimum altitude of -3000 m. Table 1 summarizes the reference altitude profiles taken for the model.

A difference in altitude produces a difference in equilibrium temperature that,

Altitude (m)	-6000	0	**1000**	2000
Defrost mass (kg.m^{-2})	107	152	159	166

Table 2
Altitude effect on defrost mass balance at latitude 55°S. The defrost mass model is used for the SSPC anti-cryptic sector recession with the time independent albedo scenario (model M2) discussed in section 4.1.8.

Altitude (m)	1500	**2500**	3500
Defrost mass (kg.m^{-2})	1214	1201	1189

Table 3
Same as table 2 at latitude 85°S.

in turns, leads to a difference of thermal emission and thus of defrost mass balance. We solve the equation of energy balance at the surface (see section 3.3.1) for the cryptic and anti-cryptic sectors at four latitude points : 55°S, 65°S, 75°S, 85°S. We use the empirical law of time independent but latitude dependent albedo (model M2) as discussed in section 4.1.8. Emissivity is set to 0.99 in order to maximize the effect of altitude on the defrost mass.
At latitude 55°S (table 2) a difference of ± 1000 m in altitude, leads to a difference in defrost mass of ± 7 kg.m^{-2} (± 4.4% of the total mass sublimated during the recession phase) and thus a shift of the crocus date of ± 1 °Ls. At 85°S, the difference in defrost mass represents ± 12 kg.m^{-2} , i.e. ± 1.1% of the total mass, and thus a shift of the crocus date of ± 0.6 °Ls. (table 3). For comparison, the observed difference in crocus date, which is about 20° of Ls at 85°S, corresponds to a defrost mass of 300 kg.m^{-2}.

In conclusion, the small altitude differences of ≈ 1000 m between the cryptic and anti-cryptic sectors are not enough to explain the SSPC recession asymmetry.

4.1.5 Radiation on a rough surface

This section presents a sensitivity study of our model regarding surface roughness. In order to estimate the effect of slope and shadow induced by surface roughness on the daily average absorbed radiation W (equation 3), we compute it using the parametrization presented in section 3.2. We choose the following configuration : $A_{vis} = 0$, $A_{IR} = 0.01$ and $\varepsilon = 0.99$ to maximize the effect of slope and shadow.

Figure 4 represents the meridian profiles of W as a function of Ls for the cryptic and anti-cryptic ranges of longitudes. One can see that the spatio-temporal pattern of W is nearly identical for both sectors despite the fact that the distribution of the facets orientation as well as the roughness of the terrains could be different. This suggests that these factors do not play a role at first order

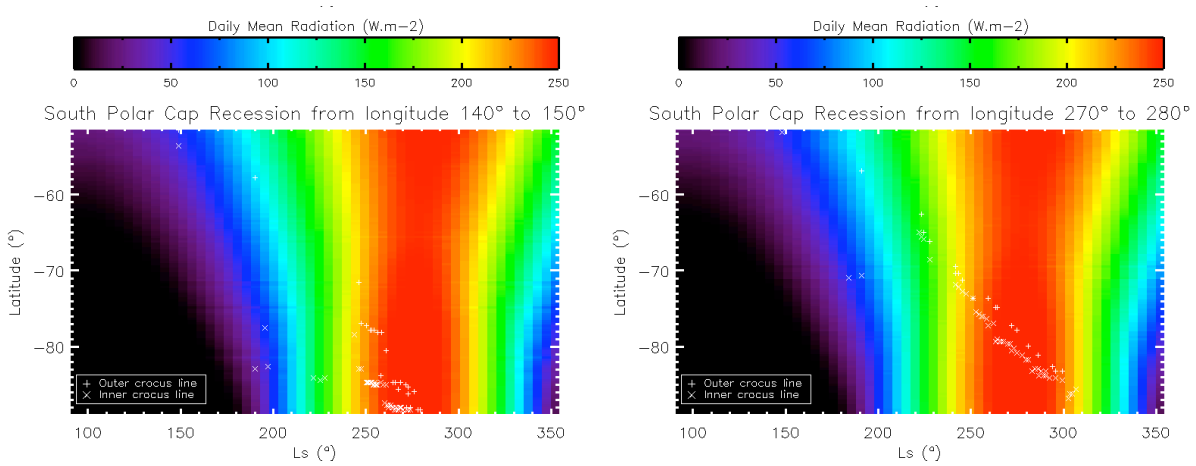

(a) (b)

Figure 4. SSPC crocus lines (symbols) for one meridian profile of the cryptic sector (140°-150°E) and one for the anti-cryptic sector (270°-280E) compared to the spatio-temporal pattern of the mean daily absorbed radiation W (gray scale) for an albedo of 0.

in the asymmetry.

4.1.6 Emissivity and albedo in the thermal infra-red

Emissivity and albedo are linked through the Kirchhoff's law :

$$A_{IR}(\theta, \lambda) = 1 - \varepsilon(\theta, \lambda) \tag{22}$$

with θ the zenith angle and λ the wavelength. The directional hemispheric albedo for a beam of light with incidence θ is noted $A_{IR}(\theta, \lambda)$. The emissivity at the emergence angle θ is noted $\varepsilon(\theta, \lambda)$.

Neither the emissivity nor the albedo of the surface of Mars in the thermal infrared can be directly measured from space because of ambiguities with temperatures. Nevertheless, some estimation of emissivity using the band ratio $\varepsilon = 1 - BD_{25}$ with TES measurements has been done by Eluszkiewicz and Moncet, 2003. This study shows that, during the first year covered by MGS (martian year 25), the emissivity stays at levels higher than 0.9 for the polar region after Ls=140°. A small asymmetry in emissivity is apparent at this date and then tends to disappear.

Theoretical studies or laboratory measurements provide some other clues. Warren et al., 1990 propose to model CO_2 ice spectral emissivity using the Mie theory applying the delta-Eddington approximation and using laboratory measured optical constants. Emissivity is weighted by the Planck function for

a temperature of 148K, representative of the SSPC CO_2 frost temperature and averaged from 6 to 25 microns. This spectral domain contain only half of the black body energy but no optical constants were available at wavelengths longer than 25 microns. For pure CO_2 ice, the emissivity increases with grain size, ranging from 0.29, for of 5 microns grain size, to 0.91, for 2000 microns. As discussed by Langevin et al., 2007, the grain size of SSPC CO_2 observed by OMEGA ranges from a few mm to several 10 cm, leading to an emissivity higher than 0.91. Warren et al., 1990 also show that the presence of dust and water ice increase the emissivity. Local variability of grain size, water ice and dust content can lead to differences in emissivity from 0.91 (pure CO_2 ice with grain size of 2 mm) to 1.0 (maximum value).

We will use the range of emissivity from 0.91 to 0.99 in agreement with both TES measurements and theoretical considerations.

To estimate accurately the effect of emissivity, we simulate the cumulative frost sublimation mass, by solving the equation of energy balance at the surface (see section 3.3.1), for the anti-cryptic sector at two extreme altitudes and latitude. At 85°S, the cumulative defrosted mass with $\varepsilon = 0.99$ (resp. $\varepsilon = 0.91$) is 1213 kg.m^{-2} (resp. 1242 kg.m^{-2}). This difference represents 1.6% of the total mass sublimated during the recession phase, and accelerates the crocus date by a shift of -1.6°Ls. At 55°S, the cumulative defrosted mass with $\varepsilon = 0.99$ (resp. $\varepsilon = 0.91$) is 159 kg.m^{-2} (resp. 177 kg.m^{-2}). This difference represents 13% of the total mass, and should accelerate the crocus date by a shift of -2.4°Ls. These values are small compared to the difference in crocus date ≈20° between the cryptic and anti-cryptic sectors.

In conclusion, the effect of emissivity is negligible in the asymmetry of the SSPC recession.

4.1.7 Albedo in the visible range

As an approximation, we identify the bolometric albedo A_{vis} in the visible with the OMEGA reflectance at 1.07 microns (see section 2.4). We thus implicitly assume that the variability of the latter with the observation conditions (observation geometry, lighting condition, atmospheric load) is weak compared to the variability linked with the surface physical properties.

In order to be compatible with our model, we average the observed OMEGA albedo for each bin, according to our reference grid (section 3.4) with a integration time step of Ls=5°. This albedo is noted A^O_{vis}.

Different investigations conducted in the visible and in the near IR have shown that the SSPC is asymmetric in albedo (James et al., 1979; Kieffer et al., 2000). Figure 5 shows that OMEGA measurements confirm this conclusion.

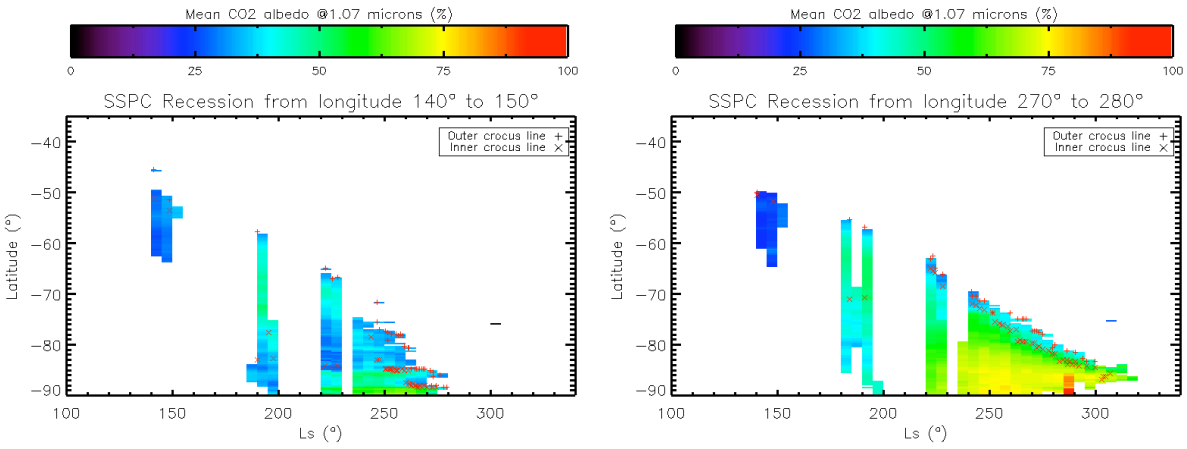

(a) (b)

Figure 5. SSPC crocus line (symbols) compared to the spatio-temporal pattern of mean local albedo A^O_{vis} (gray scale) for two meridian profiles : the cryptic (140°-150°E) and anti-cryptic (270°-280E) sectors.

The A^O_{vis} of the cryptic sector is 20 - 60 % lower than the albedo of the anti-cryptic sector. This leads to a sublimation rate that can be up to three times higher. The contrast is particularly clear after Ls=220°. Before this date there could be an effect of water ice clouds, which are present everywhere over the cap (Langevin et al., 2007), that could smooth the spatial variations of the reflectance at 1.07 microns. Optical depth of the clouds on OMEGA data has not yet been systematically constrained and, consequently, is not taken into account in this study.

We observe that the crocus date at latitude 85°S occurs 29°Ls later at 270°-280°E longitude than at 140°-150°E. This seems to be very well correlated with the difference in observed albedo (figure 5). In addition the divergence, between the cryptic and anti-cryptic sectors, of the albedo evolution and the crocus line recession occur nearly simultaneously at Ls≈220° (see section 4.1). Therefore albedo seems to be a good candidate to explain the asymmetry in the SSPC recession. This qualitative result will be tested quantitatively in the next section. The origin of the albedo asymmetry - such as frost deposition, dust content, cleaning process, slab ice - will be discussed in section **??**.

4.1.8 Quantitative test

We test the global coherence between the model (described in sections 3.2 and 3.3), the mean latitudinal propagation of the crocus line with time $T^O_{end}(L', \phi)$ (see fig 2), the albedo A^O_{vis} measurements by OMEGA (see section 2.4) and the GRS and HEND net CO_2 latitudinal accumulation curves $M^H_{CO_2/tot}(\phi)$ at the end of winter (Litvak et al., 2007; Kelly et al., 2006). As before, we consider two reference sectors of longitude (cryptic and anti-cryptic).

The albedo $A_{vis} = A_{vis}(L, \phi, Ls)$ is a field depending on longitude, latitude and time (expressed here in °Ls) that it is only sampled sparsely in space and time by our observations. As a consequence we parametrize A_{vis} using simple laws for its dependencies with latitude and time, according to two basic scenarii:

- Time independent albedo (model M2) : $A_{vis}(L, \phi, Ls) = A^{M2}_{vis}(L', \phi)$; L' represents the considered longitude sector domain : cryptic or anti-cryptic. This scenario assumes that the seasonal polar cap has latitudinal variations of albedo that does not change with time (Ls). We reproduce different regression speeds of the crocus line by modulating the latitudinal distribution of energy absorbed by the frost since the beginning of the sublimation phase. For instance, an acceleration of the crocus line corresponds to the crossing of a region with a lower albedo than the adjacent regions at lower latitude.
- Latitude independent albedo (model M3) : $A_{vis}(L, \phi, Ls) = A^{M3}_{vis}(L', L_s)$; same definition for L'. This scenario assumes that the seasonal polar cap has a constant latitudinal albedo but that does change with time (Ls). We reproduce different regression speeds of the crocus line according to time and longitude by modulating the temporal repartition of the energy absorbed by the frost since the beginning of the sublimation phase. For instance, an acceleration of the crocus line corresponds to a simultaneous decrease of the albedo for the whole remaining cap.

In both cases we consider flat and horizontal but use realistic altitudes.

4.1.8.1 Time independent Albedo (model M2) For a given latitude ϕ, we compute the *equivalent albedo* $A^{M2}_{vis}(L', \phi)$ required to sublimate the CO_2 frost initial mass $M^{H}_{CO_2/tot}(\phi)$ measured by HEND/GRS, in the interval of time $[T^{M2}_{beg}(L', \phi), T^{O}_{end}(L', \phi)]$. The date $T^{M2}_{beg}(L', \phi)$ is the beginning of the net sublimation, when the local mass balance becomes negative in our model (equation 17) in this time independent albedo scenario, whereas $T^{O}_{end}(L', \phi)$ is the crocus date determined by OMEGA (end of the sublimation phase, fig. 2). The error bar on the equivalent albedo is mainly defined by the error bar on the initial mass. We use an high emissivity, $\varepsilon = 0.99$, and a low albedo in the thermal IR, $A_{IR} = 0.01$, in order to estimate the lower limit of the equivalent albedo. We show in section 4.1.6 that the effect of emissivity in its realistic range of occurrence (between 0.91 and 1) is minor on the defrost mass and thus on the equivalent albedo.
We test the validity of the model by evaluating : (i) the agreement between the equivalent albedo $A^{M2}_{vis}(L', \phi)$, estimated for the four latitudes at 85°S, 75°S, 65°S and 55°S in concordance with the HEND study (Litvak et al., 2007), and the observed albedo $A^{O2}_{vis}(L', \phi) = \left\langle A^{O}_{vis}(L', \phi, Ls) \right\rangle)$, averaged over the whole recession period. (ii) the agreement between $T^{H}_{beg}(\phi)$, the date of the beginning of the net sublimation according to HEND, and this same date $T^{M2}_{beg}(L', \phi)$, according to the model.

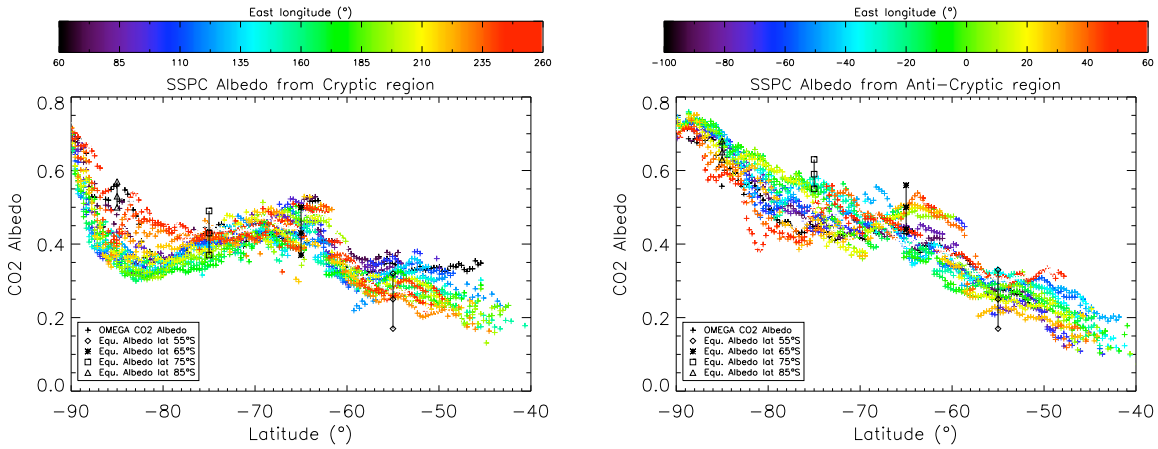

Figure 6. Evaluation of time independent scenario (model M2) for both cryptic and anti-cryptic sectors. Black "symbols" : equivalent albedo $A_{vis}^{M2}(L', \phi)$ required to sublimate the frost observed by HEND and GRS. Errors bars in albedo are due to the CO_2 thickness measurement. Color "+" : Averaged albedo $A_{vis}^{O2}(L', \phi)$ of CO_2 (colors represent the longitude) measured by OMEGA.

The first evaluation (i) can be done be analyzing figure 6, showing albedo vs latitude for both sectors.
For both reference sectors, there is a general agreement between $A_{vis}^{M2}(L', \phi)$ and the time averaged albedo $A_{vis}^{O2}(L', \phi)$ observed by OMEGA (fig. 7). Albedo increases with latitude, much stronger for the anti-cryptic sector than for the cryptic sector.

The second evaluation (ii) is done through the analysis of tables 4 and 5. We can analyze the match between $T_{beg}^{H}(\phi)$ and $T_{beg}^{M2}(L', \phi)$ as an indicator of the validity of our scenario. The agreement is relatively good at low latitude ϕ for both sectors L'. The misfit increases as latitude increases.

In conclusion there is an acceptable coherence, trough the model, of several datasets: albedos observed by OMEGA, crocus lines observed by OMEGA, net accumulation measured by HEND/GRS and altitudes measured by MOLA. The disagreement on the date of the beginning of sublimation at high latitudes is the main argument against this scenario. Moreover the low spatial sampling in latitude of the HEND/GRS measurements do not favor the testing of this model.

4.1.8.2 Latitude independent albedo (model M3) This second scenario (model M3) is based on a simple model of albedo $A_{vis}^{M3}(L', L_s)$ depending on longitude (cryptic/anti-cryptic) and time. Such a scenario seems to be more accurate than the previous one because it has no limitation of the latitude sampling required by HEND/GRS. We determine two empirical laws of temporal evolution for the albedo of the cryptic and anti-cryptic sectors (fig. 7). This

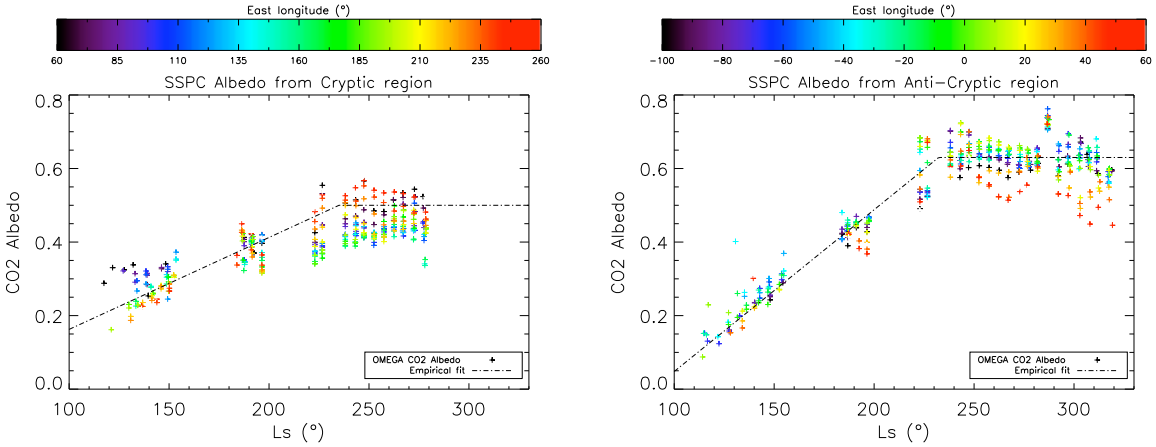

Figure 7. Empirical law of albedo for the latitude independent scenario (model M3) for both cryptic and anti-cryptic sectors. Color "+" : latitude averaged albedo $A^{O3}_{vis}(L', Ls)$ of CO_2 ice (gray scales represent longitude) measured by OMEGA. Doted line : empirical fit $A^{M3}_{vis}(L', Ls)$.

law for the cryptic sector (longitudes between 60° and 260°E) is :

$$A^{M3}_{vis}(Ls) = \min\left(0.35 + \frac{0.15}{60}(Ls - 175), 0.5\right) \tag{23}$$

For the anti-cryptic sector (longitude between 100°W and 60°E) :

$$A^{M3}_{vis}(Ls) = \min\left(0.40 + \frac{0.22}{50}(Ls - 180), 0.63\right) \tag{24}$$

The albedo increases with time until Ls=230°. The increase is much larger for the anti-cryptic sector than for the cryptic sector. Both laws fit well the observed albedo $A^{O3}_{vis}(L', Ls) = \left\langle A^{O}_{vis}(L', \phi, Ls)\right\rangle)$ averaged in latitude, as a function of time (fig. 7).

We test the validity of this scenario by evaluating: (i) the agreement between the sublimated CO_2 mass $M^{M3}_{CO_2/tot}(L', \phi)$ predicted by the model M3, and the mass $M^{H}_{CO_2/tot}(\phi)$ measured by GRS/HEND ; (ii) the agreement between the date $T^{M3}_{beg}(L', \phi)$ the date of the beginning of the net sublimation according the model M3, and $T^{H}_{beg}(\phi)$, the same according to HEND.

We invite the reader to perform the first evaluation (i) by studying tables 4 and 5. The mass $M^{M3}_{CO_2/tot}(L', \phi)$ predicted by the model fits well within the error-bar of the measured masses $M^{H}_{CO_2/tot}(\phi)$ except for one point : at latitude -85°S in the cryptic sector.

Our prediction overestimates the observation by 143 kg.m^{-2} while the error bar is only 100 kg.m^{-2}. If this is significant, it can be attributed to an

underestimation of albedo but considering fig 7, albedo seems to be already overestimated ! One hypothesis could be that the accumulation is not strictly symmetric around the geographic south pole.

The second evaluation (ii) can be done using the same tables 4 and 5. The agreement between $T^{H}_{beg}(L', \phi)$ and $T^{M3}_{beg}(L', \phi)$ is good at low latitudes for both sectors. However the misfit increases as latitude increases. Again, the explanation is that the spatio-temporal behavior of the albedo is more complex than the two basic scenarii we have investigated as can be seen in figure 5. The latitude independent scenario M3 seems to be more relevant than the time independent scenario M2 because it has not the limitation of the coarse latitude sampling imposed by GRS.

In conclusion, confronting the model to the observations shows that the albedo is the most determinant parameter and that it increases globally during the recession for both (albeit differently) the cryptic and anti-cryptic sectors. The relative agreement between the model and the observations, in particular for the cryptic sector, suggests that all the solar energy absorbed by the mineral substrate underlying the CO_2 ice slab and/or the upper layer of dust contamination should be transferred to the CO_2 deposits for their sublimation.

4.2 SSPC Recession at local scale

Already at the end of the XIXth century, the irregular SSPC waning was noticed with telescope observations by Campbell (1895). Using Mariner 9 photographs, Veverka and Goguen, 1973 concluded that the surface topography controls this irregularity. We quantify here the structure of the edge of the SSPC by the snowdrop distance evaluated by meridian profile of CO_2 detection by OMEGA.

In section 2.3 we define the inner and outer crocus lines for a given date (Ls) as well as the inner and outer crocus dates for a given latitude. The time elapsed between these two dates is the snowdrop time. According to OMEGA CO_2 ice detection, the snowdrop time ranges from a few °Ls to more than 40°Ls depending on space and time. In this section, we will discuss the origin of this phenomenon.

We will address the following key question. Is the local variability of snowdrop time due to local variations at spatial scales of typically 1 km of: accumulation ? subsurface annual heat wave ? CO_2 ice stability linked with altitude differences ? radiation absorption controlled by roughness ? difference in albedo in the visible range ? difference in emissivity/albedo IR ? For that purpose we seek correlations between the snowdrop time and the local variability of the

	Latitude	55°S	65°S	75°S	85°S
HEND+GRS	Mass [kg.m^{-2}] $M^{H}_{CO_2/tot}(\phi)$	180±40	450±80	750±100	1050±100
-	Sublimation duration [°Ls] $T^{H}_{beg}(\phi)/-$	140/ -	160/ -	170/ -	180/ -
Model M2	Sublimation duration [°Ls] $T^{M2}_{beg}(L',\phi)/T^{O}_{end}(L',\phi)$	135/170	165/220	185/245	200/270
-	Equivalent albedo [1] $A^{M2}_{vis}(L',\phi)$	0.25	0.43	0.43	0.53
-	Min/Max equ. albedo [1] $A^{M2}_{vis}(L',\phi)$	0.17/0.32	0.50/0.37	0.49/0.37	0.57/0.50
Model M3	Mass [kg.m^{-2}] $M^{M3}_{CO_2/tot}(L',\phi)$	154	482	687	1193
-	Sublimation duration [°Ls] $T^{M3}_{beg}(L',\phi)/T^{O}_{end}(L',\phi)$	135/170	165/220	185/245	195/270
Model M1(I=20)	Subsurface heat [kg.m^{-2}]	0.5	0.5	0.6	0.6
-	Sublimation duration [°Ls] $T^{H}_{beg}(\phi)/T^{M1}_{end}(L',\phi)$	140/185	160/235	170/260	180/280
Model M1(I=1000)	Subsurface heat [kg.m^{-2}]	12	24	29	21
-	Integration duration [°Ls] $T^{H}_{beg}(\phi)/T^{M1}_{end}(L',\phi)$	140/155	160/215	170/245	180/265

Table 4
Models for the SSPC recession in the cryptic sector. The first two lines are the measurements by HEND/GRS. The next three lines summarize the results of the time independent albedo scenario (model M2). The next two lines summarize the latitude independent albedo scenario (model M3). The last four lines give to the subsurface heat released by the annual heat wave (model M1) as exposed in section 4.1.3.

previous parameters.

4.2.1 Statistical index

The inner and outer crocus lines are defined on the basis of spatial bins. The appearance of the first 1% defrosted pixels defines the inner crocus date whereas the disappearance of the last 1% frosted pixels defines the outer crocus date. Thus the snowdrop time, is a measure of the time elapsed between these two extreme defrost situations. In other words, the snowdrop time is an estimation of the distribution width of T_{end} inside the bin. Such a distribution

	Latitude	55°S	65°S	75°S	85°S
HEND+GRS	Mass [kg.m^{-2}] $M^{H}_{CO_2/tot}(\phi)$	180±40	450±80	750±100	1050±100
-	Sublimation duration [°Ls] $T^{H}_{beg}(\phi)/-$	140/-	160/-	170/-	180/-
Model M2	Sublimation duration [°Ls] $T^{M2}_{beg}(L',\phi)/T^{O}_{end}(L',\phi)$	135/170	170/225	190/260	205/290
-	Equivalent albedo [1] $A^{M2}_{vis}(L',\phi)$	0.25	0.5	0.59	0.65
-	Min/Max equ. albedo [1] $A^{M2}_{vis}(L',\phi)$	0.17/0.33	0.44/0.56	0.55/0.63	0.63/0.68
Model M3	Mass [kg.m^{-2}] $M^{M3}_{CO_2/tot}(L',\phi)$	159	449	743	947
-	Sublimation duration [°Ls] $T^{M3}_{beg}(L',\phi)/T^{O}_{end}(L',\phi)$	135/170	165/225	185/260	205/290
Model M1(I=20)	Subsurface heat [kg.m^{-2}]	0.5	0.6	0.7	0.5
-	Sublimation duration [°Ls] $T^{H}_{beg}(\phi)/T^{M1}_{end}(L',\phi)$	140/185	160/245	170/280	180/315
Model M1(I=1000)	Subsurface heat [kg.m^{-2}]	12	27	29	27
-	Integration duration [°Ls] $T^{H}_{beg}(\phi)/T^{M1}_{end}(L',\phi)$	140/155	160/215	170/245	180/265

Table 5
Same as table 4 but for the SSPC recession models in the anti-cryptic sector.

is a function of three distributions : the initial CO_2 mass$M_{CO_2/tot}$, the date of the beginning of the sublimation T_{beg} and the mass flux of sublimation $\frac{\partial M_{CO_2}}{\partial t}$. If these distributions inside the bin are narrow, all facets will defrost almost at the same time and the snowdrop time will be short. On the contrary, if these distributions inside the bin are wide, all facets will defrost at different times and the snowdrop time will be large. In short, the snowdrop time must be correlated with a combination of these three distributions: $M_{CO_2/tot}$, T_{beg}, $\frac{\partial M_{CO_2}}{\partial t}$.

We propose to describe the distribution width of the random variable X, with N occurrences named X_i, with the following statistical parameter :

$$\hat{P_{stat}}(\mathrm{X}) = \frac{\sqrt{\hat{\sigma}}}{\hat{\mu}} \tag{25}$$

$\hat{\mu}$ and $\hat{\sigma}$ being the usual estimators of the mean and variance :

$$\hat{\mu} = \frac{1}{N}\sum_{i=1}^{N} \mathrm{X_i} \tag{26}$$

$$\hat{\sigma} = \frac{1}{N-1}\sum_{i=1}^{N} (\mathrm{X_i} - \hat{\mu})^2 \tag{27}$$

Now we define a statistical index $R_{stat}(\mathrm{X})$ that describes the discrepancy between the lower and upper parts of the population of distribution of X. Let suppose that X is Gaussian, 32% of the population should be outside the range $[\hat{\mu} + \sqrt{\hat{\sigma}}, \hat{\mu} - \sqrt{\hat{\sigma}}]$: 16% in the bottom wing and 16 % in the top wing. The lower limit of the ratio between an occurrence of the upper population and an occurrence of the lower population is :

$$R_{stat} = \frac{\hat{\mu} + \sqrt{\hat{\sigma}}}{\hat{\mu} - \sqrt{\hat{\sigma}}} = \frac{1 + \hat{P_{stat}}}{1 - \hat{P_{stat}}} \tag{28}$$

Let suppose that $M_{CO_2/tot}$ and T_{beg} take a unique value. If we estimate that $\hat{P_{stat}}$ for the defrost mass flux $\frac{\partial M_{CO_2}}{\partial t}$ inside a bin is equal to 0.4, it means that 16% of the population (upper wing) will have a sublimation time duration T_{end} half of other 16% (lower wing).

Now we must test the correlation, for a given latitude and longitude range, between the snowdrop time (distribution width of T_{end}) and the the statistical index $\hat{P_{stat}}$ of : (i) the initial accumulated mass $M_{CO_2/tot}$; (ii) the date of the beginning of the sublimation T_{beg} ; (iii) the mass flux $\frac{\partial M_{CO_2}}{\partial t}$ or any any physical parameter that controls it. In the special case of the albedo (that control partly $\frac{\partial M_{CO_2}}{\partial t}$), we sort all pixels of the OMEGA observations from Ls=0° to 360° in the bins of our geographical grid (see section 3.4) and by intervals of 5° Ls. Then we calculate for each bin containing pixels the mean $\hat{\mu}$, the variance $\hat{\sigma}$ and the statistical index $\hat{P_{stat}}$ of the albedo. .

4.2.2 CO_2 *ice accumulation:* $M_{CO_2/tot}$

The total CO_2 ice accumulation, previously discussed at global scale in section 4.1.1, can vary at local scale.
According to equation 21, the local scale variation of accumulation depends on different terms that can have a local expression : (i) thermal emission controlled by temperature and emissivity ; (ii) atmospheric heat advection ; (iii) subsurface heat conduction which depends on slope, albedo and thermal inertia of the subsurface; (iv) absorbed radiation linked with the VIS and IR albedos, slope, and roughness.

The accurate modeling of accumulation at local scale, including atmospheric dynamic effects, is out of the scope of this paper. Thermal inertia observed by TES is uniform near the South pole (Putzig et al., 2005). In this study, we will suppose that accumulation varies smoothly with latitude, as measured by HEND (Litvak et al., 2007). This apparent smoothness could be an effect of the large instrument footprint. Thus ambiguities between $M_{CO_2/tot}$ in one hand, and T_{beg}, $\frac{\partial M_{CO_2}}{\partial t}$, in the other hand, will not be resolved properly in this work.

4.2.3 Date of the beginning of sublimation: T_{beg}

As discussed in section 4.1.2, T_{beg} is related to the all terms of equation 21. In the next models, T_{beg}will be an free parameter, fixed by the model itself.

4.2.4 Annual heat wave in the ground

As previously discussed in section 4.1.3, the maximum sublimated mass due to the annual heat wave in the ground represents 6% of the total sublimated mass (at latitude 55°S) leading to a shift of the crocus date of less than 2°Ls. For comparison, the maximum snowdrop time is more than 40°Ls. This energy source can thus be neglected at first order in all discussions concerning the recession phase even at local scale.

4.2.5 Altitude

The effect of altitude, as previously discussed in the section 4.1.4, is very low at global scale. At local scale, the typical standard deviation of altitude inside a bin is between 10 m and 1000 m. We estimated the effect of 1000 m difference in altitude for two extreme point of the anti-cryptic sector : At 85°S an increase in altitude of 1000 m from the 2500 m level leads to a decrease of defrosted mass of 13 kg.m^{-2} during the complete recession time. The corresponding snowdrop time delay is 0.5°Ls. At 55°S from the 1000 m level, the defrosted mass decrease represents 7 kg.m^{-2} and a snowdrop time delay of 1°Ls, much less than most of the observed snowdrop time. The altitude effect alone is not sufficient to explain the snowdrop time evolution in space and time.

4.2.6 Radiation budget on a rough surface

In order to estimate the effect of surface roughness on the local daily absorbed radiation W (equation 3), we compute it using the model presented in section 3.2. We set the albedos $A_{vis} = 0$, $A_{IR} = 0.01$ and the emissivity $\varepsilon = 0.99$, a

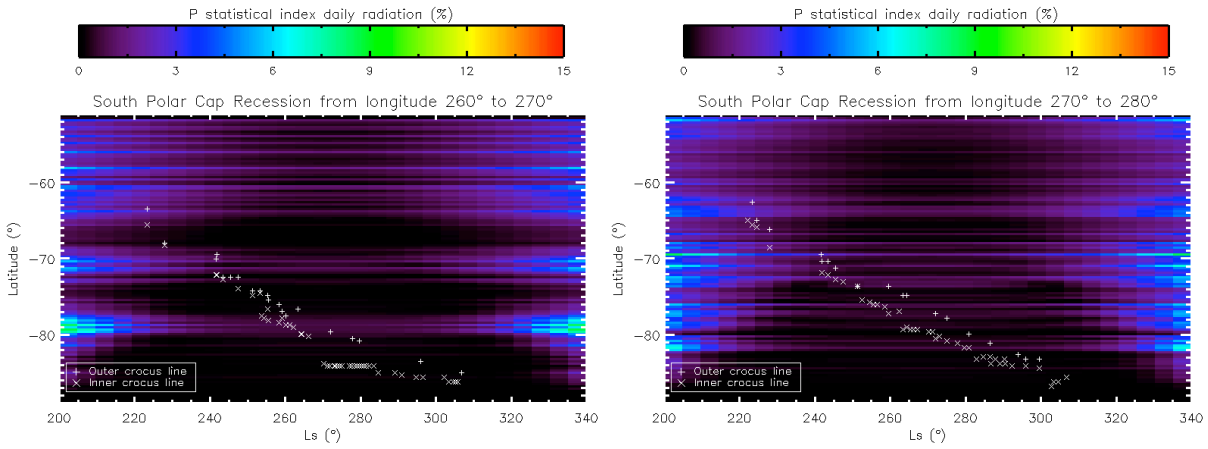

(a) (b)

Figure 8. SSPC recession compared to local radiation modulated by surface roughness for two meridian profiles : over longitudes (a) 260°-270°E and (b) 270°-280E. Symbols represent the inner and outer crocus lines. The gray scale represent the statistical index $\hat{P_{stat}}$ (equation 25) of the local absorbed radiation W with a special configuration that maximize the effect of surface roughness (see text).

configuration that maximizes the effect of slope and shadow on all the radiation terms. Slope and altitude given by the MOLA database are at a resolution of 920 m. If roughness of the martian surface is the parameter that controls the recession at local scale, the snowdrop time and the local statistical index $\hat{P_{stat}}$ for the daily absorbed radiation must correlate. Figure 8 represents the statistical index $\hat{P_{stat}}$ along two meridian profiles (a) 260°-270°E and (b) 270°-280°E.

First we can note that the effect of slope distribution on the variability of absorbed radiation is particularly noticeable when the sun elevation at local noon is low. On profile (a), the maximum snowdrop time (about 30°Ls) occurs at latitude 85°S but does not correlate with high values of the statistical index $\hat{P_{stat}}$. On profile (b), the snowdrop time is constant (about 10°Ls) despite the fact that the statistical index at the crocus line decreases with time. It seems that the snowdrop time is independent of the local absorbed radiation modulated by surface roughness. This result stands for all other directions around the south geographic pole.

In order to completely reject the hypothesis of surface roughness effect, the snowdrop time must be compared with the local distribution of defrost mass rather than radiation budget. Section 4.2.9 will discuss this point.

4.2.7 Emissivity and albedo in the thermal infra-red

As discussed in section 4.1.6, emissivity ranges from 0.91 to 1.0 for the CO_2 ice. Using the same calculation at both 85°S and 55°S, we can estimate the effect of emissivity distribution on snowdrop time. If emissivity is distributed between these the two extreme values, the snowdrop time is increased by 1.6°Ls at 85°S and 2.4°Ls at 55°S. This is not enough to explain the local variations in snowdrop time. Emissivity cannot be the key parameter that controls the SSPC recession at local scale.

4.2.8 Albedo in the visible range

In order to estimate the effect of albedo on the snowdrop time, we estimate its distribution from our selection of OMEGA observations arranged into bins. We use the absorption factor $Abs_{vis} = 1 - A_{vis}$ that appears in equation 5. As an approximation we identify A_{vis} with the reflectance $R^O_{1.07}$ at 1.07 microns observed by OMEGA (see section 2.4) - ie : we assume a lambertian behavior of the surface reflectance. If the albedo is the parameter that controls the recession at local scale, snowdrop time and the local statistical index $\hat{P_{stat}}$ of Abs^O_{vis} must be correlated.

We choose to represent in figure 9 six typical meridian profiles to illustrate the test of our hypothesis : (a) 0°-10°E , (b) 70°-80°E , (c) 200°-210°E , (d) 260°-270°E , (e) 270°-280°E and (f) 320°-330°E. We restrict the time window of this investigation to Ls=220°-330° because, before Ls=220° pollution by atmospheric dust and water ice is likely (see section 2.4) and their contribution to $R^O_{1.07}$ will affect its representativity of the surface albedo.

On profile (a), the snowdrop time is maximum (about 40°Ls) at 84°S and correlates with a high value of $\hat{P_{stat}}$ present at this latitude since Ls=255°.

On profile (b), the snowdrop time is intermediate (about 15°Ls) from 75°S to 83°S, where $\hat{P_{stat}}$ is low. At latitudes between 83°S and the pole, the snowdrop time reaches 30°Ls and is well correlated with a local large $\hat{P_{stat}}$.

Profile (c) presents an uniform snowdrop time of about 10-15°Ls and the estimation of $\hat{P_{stat}}$ is low.

On profile (d) from latitude 84°S to 86°S and since Ls =220°, albedo is very dispersed with high $\hat{P_{stat}}$ values. This is correlated with a very high snowdrop time of more than 30°Ls.

Profile (e) shows the most homogeneous snowdrop time (10°Ls) of all profiles around the south pole, in agreement with constantly low levels of $\hat{P_{stat}}$.

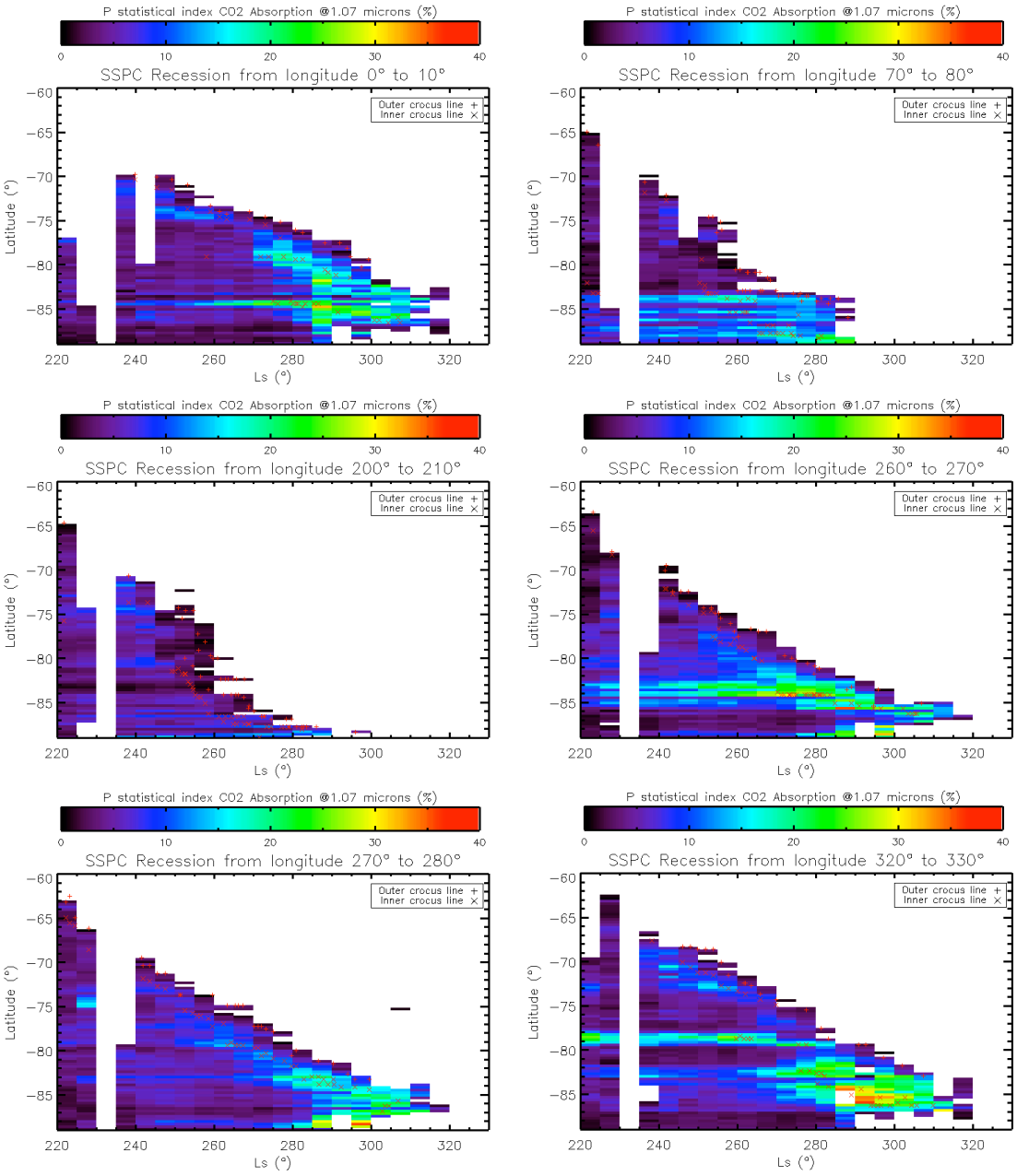

Figure 9. SSPC recession compared to the albedo distribution observed by OMEGA for six meridian profiles: (a) 0°-10°E, (b) 70°-80°E , (c) 200°-210°E, (d) 260°-270°E, (e) 270°-280°E and (f) 320°-330°E. Symbols represent the inner and outer crocus lines. The gray scale represents the statistical index $\hat{P_{stat}}$ (equation 25) of the local absorption factor Abs^{O}_{vis} inside each bin.

On profile (f), we note three very distinct regimes of albedo dispersion. At latitudes below 78°S, $\hat{P_{stat}}$ is close to zero. Between 78°S and 80°S, $\hat{P_{stat}}$ is higher than 20% since Ls=220°. Between 82°S and 87°S $\hat{P_{stat}}$ increases with time. This is correlated with a low snowdrop time for the first part (less than 10°Ls), and a high snowdrop time (more than 20°Ls) for the second as well as

the third regimes.

Another phenomenon occurs on all profiles, as suggested by the close examination of $\hat{P_{stat}}$: the albedo dispersion increases just before the transition zone. This is easily explained by the fact that subpixel mixing occurs at this time and that OMEGA see pixels with various levels of sub-pixel mixing, and thus various albedo, all with positive detection of CO_2. This is particularly obvious on profiles (a), (d), (e) and (f) where the global albedo level is high and the subpixel mixing can produce a high variance.

Local dispersions of albedo show a quasi-systematic correlation with the snowdrop time. This result is also valid for all other directions around the south geographic pole. We conclude that albedo is likely the key parameter that control the SSPC recession at local scale.

4.2.9 Quantitative test

In sections 4.2.4 to 4.2.8 we have shown that :

- local variations of subsurface heat flow, altitude and emissivity cannot control alone the snowdrop time for a given latitude since their influence on the cumulative mass of sublimated CO_2 is weak compared to the influence of other factors.
- the snowdrop time is well correlated with the local variability of albedo whereas it is not with the absorbed radiation variability due to the slope distribution alone.

In order to confirm the prevailing nature of the albedo we perform a more detailed simulation of the cumulative mass of sublimated CO_2 frost for each facets of our geographical grid. We take the altitudes and slopes from the MOLA data at a resolution of 920 m. At contrary we ignore the local variation of the albedo by taking a homogeneous value that increases with time, i.e.: latitude independent scenario, model M3 (see section 4.1.8) for the whole cap. At global scale such a simplified model allowed us to reproduce the recession of the mean crocus line (section 4.1.8). All the other parameters are set to the standard values given in section D.
If surface roughness is the parameter that controls the recession of local scale, snowdrop time and the local statistical index $\hat{P_{stat}}$ of the daily defrost mass $\frac{\partial M_{CO_2}}{\partial t}$ must be correlated.

In figure 10 we choose to represent the spatio-temporal behavior of $\hat{P_{stat}}$ for the six meridian profiles and the time window already considered in section 4.2.8: (a) 0°-10°E, (b) 70°-80°E, (c) 200°-210°E, (d) 260°-270°E, (e) 270°-280°E and (f) 320°-330°E.

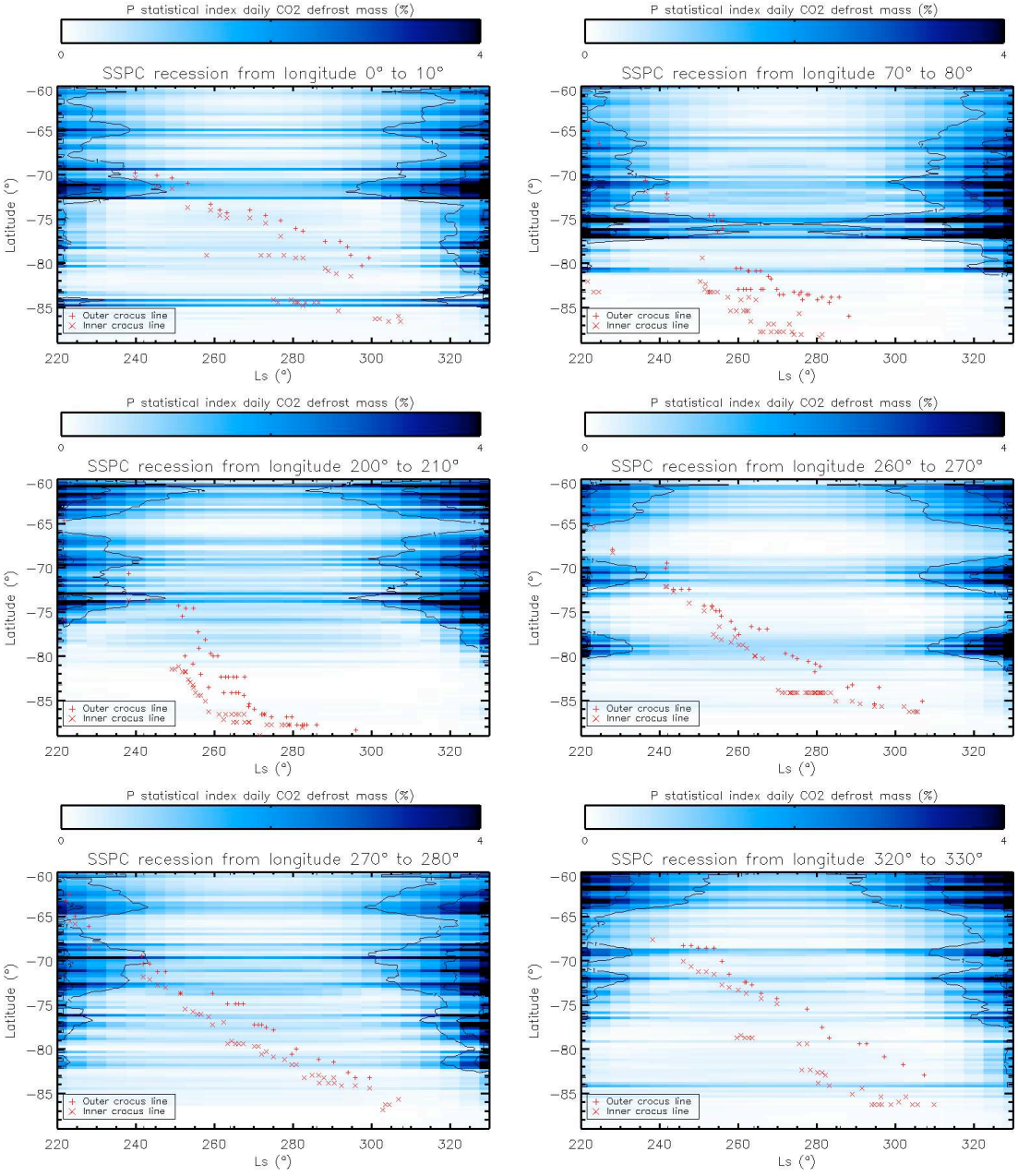

Figure 10. SSPC recession compared to sublimated CO_2 mass distribution computed for six meridian profiles : (a) 0°-10°E , (b) 70°-80°E , (c) 200°-210°E , (d) 260°-270°E , (e) 270°-280°E and (f) 320°-330°E. Symbols represent the inner and outer crocus lines. Colors represent the statistical index $\hat{P_{stat}}$ (equation 25) of the local daily defrosted mass $\frac{\partial M_{CO_2}}{\partial t}$ inside each bin.

On profile (a), the snowdrop time is maximum (about 40°Ls) at 84°S and is well correlated with a high value of $\hat{P_{stat}}$ already present since Ls=220°. There is also a correlation with a high dispersion of albedo (section 4.2.8) but on the other hand at 79°S, a high snowdrop time occurs with a low $\hat{P_{stat}}$.

On profile (b), the snowdrop time is intermediate (about 15°Ls) from 75°S to 83°S, when $\hat{P_{stat}}$ is latitude dependent. At latitudes above 83°S, the snowdrop time reaches 30°Ls and is anti-correlated with $\hat{P_{stat}}$.

From 80°S to 90°S, profile (c) presents an homogeneous intermediate snowdrop time of about 10-15°Ls corresponding to very low values of $\hat{P_{stat}}$.

On profile (d) from latitude 84°S to 86°S and since Ls =220°, the defrosted mass is very uniform from place to place (low values of $\hat{P_{stat}}$). This is anti-correlated with a very high snowdrop time of more than 30°Ls.

Profile (e) shows the best constant snowdrop time (10°Ls) of all profiles around the south pole despite the fact that the dispersion of defrosted mass $\hat{P_{stat}}$ strongly fluctuate with latitude.

On profile (f), no correlation between defrosted mass $\hat{P_{stat}}$ and snowdrop time appears. For instance, at latitude between 78°S and 80°S, the snowdrop time is more than 20°Ls and $\hat{P_{stat}}$ is close to zero. Very close to latitude 84°S, the statistical index $\hat{P_{stat}}$ is always higher than 2% but no increase of the snowdrop time is observed.

This quantitative test confirms that the combined effects of altitude distribution, slope distribution, and surface roughness on the defrost mass distribution is not sufficient to explain the variability of the snowdrop distance. Albedo remains the most pertinent parameter in that matter. This result stands for all other directions around the south geographic pole.

5 Discussion and conclusions

At both global and local scales, albedo is the most pertinent parameter that controls the seasonal south polar cap recession. The effect of surface roughness at a scale lower than the resolution of the MOLA data could be relevant but is not tested in this work. It may be one of the future task but taking into account the difficulties to extrapolate topography to 1 m scale (Campbell et al., 2003).

Different physical parameters can induce asymmetry or variability in the albedo field :

- Subpixel mixing: Subpixel mixing is an artifact, only relevant at local scale, that could produce an apparent albedo variability. Various mixture, inside the footprint of the OMEGA instrument, of bright frost and dark rock/dust materials naturally leads to an albedo variability.

- Grain size: As suggested by Warren et al., 1990, grain size has a strong lowering effect on albedo. In the paroxysm, the SSPC is made of a slab of pure CO_2 ice, so transparent that a large fraction of photons can reach the bottom and be absorbed by the dust layer, thus producing a low visible albedo. This extreme scenario was suggested for the cryptic region from TES data (Kieffer et al., 2000). At this point we should note that OMEGA observations also suggest the presence of slab ice outside the cryptic region (Langevin et al., 2006). For instance at latitude 59°S in the anti-cryptic region (longitude 344°E) the albedo of the icy terrains is only 20%.
- Dust content: As suggested by Warren et al., 1990, the fraction of dust within the ice deposit has a strong lowering effect on its albedo.
- Ice thickness: As suggested by Warren et al., 1990, in the case of an optically thin CO_2 granular layer, its albedo has a positive correlation with the snow depth.

Different processes can produce a local asymmetry and/or variability of these physical parameters:

5.1 Subpixel mixing

The temperature of a completely defrosted terrain can go up to 300K, a temperature that strongly increases its thermal emission in particular towards the still frozen terrains. Their sublimation is thus accelerated. One exception should be the occurrence of an optically thick but thermally thin dark materials that would overly a layer of CO_2 ice and thus be kept at low temperatures. This scenario has been as suggested by Kieffer et al., 2000 for the cryptic region.

Subpixel mixing should happen between the inner and outer crocus dates as suggested in section 4.2.8. But subpixel mixing is not a good scenario for the whole SSPC because that would lead to a recession velocity higher than observed. In the longitude sector 320°-330°E the high albedo dispersion is present at least 40°Ls before the crossing of the inner crocus line (see figure 9).

5.2 Deposition process

During the phase of CO_2 frost accumulation, the SSPC is mainly formed by direct condensation but some events of snow are also present (Forget et al., 1998). GCM studies show that a topographic forcing by the Hellas basin creates an asymmetry in the mode of deposition: precipitation events are more frequent for the anti-cryptic sector than for the cryptic sector (Colaprete et al.,

2005). This suggests that the texture should be more granular (smaller grain sizes) for the former compared to the latter. This texture difference produces a relatively higher albedo in the anti-cryptic region.

Local topographic forcing could create local variability of the snow precipitation (Colaprete and Toon, 2002), leading to a variability of grain size and ice thickness. No simulation has been done yet by GCM at local scale for the south polar region, but this effect is a good candidate to explain the local variability of albedo.

During the SSPC recession, recondensation during the night can occur and the new condensate would cover dusty ices, enhancing the albedo. This process, that likely happens at local scale, tends to decrease albedo variability.

The usual defrost mass balance proposed in section 3.3.1 can produce local differences of defrost mass due to slope orientation, shadows or altitude. However, the statistical index of these parameters is not correlated with that of albedo. This effect is thus unlikely to produce relevant thickness distribution.

5.3 Metamorphism

The metamorphism tends to increase the optical mean free path within the ice through both grain growth and ice sintering, leading to an apparent grain size larger than the physical grain size (Eluszkiewicz, 1993). Thus, the metamorphism tends to decrease the albedo. It is controlled by the temperature of the ice but can be enhanced by solar energy absorption, boosting the internal vapor transport (sublimation, recondensation).

The differential boost by differential solar energy absorption, modulated by slopes and shadows, cannot explain neither the asymmetry nor the local variability of albedo. At global scale, both cryptic and anti-cryptic sectors will undergo this effect with the same magnitude (fig 4). At local scale there is no correlation between the snowdrop time and the radiation budget distribution (fig 8 and 9).

The differential boost may be relevant only if there is a difference in albedo, controlled for instance by grain size or dust load, leading to a difference in the amount of absorbed energy. There is a strong positive feedback between albedo and metamorphism: lower albedo, induces more solar energy absorbed, induces stronger metamorphism, induces higher grain size, induce lower albedo. Such a process can enhance small differences by catastrophic events. For instance, the metamorphism may be appropriate to enhance initial asymmetry due to grain size or initial local variability due to difference in dust load.

5.4 Dust precipitation

The dust content within the ice deposit can be incorporated during the accumulation phase or can be added later due to dust precipitation.

Different scenarii could imply various dust sources such as the atmosphere or local geysers. If dust particles have an aeolian origin, they can be deposited in variable amount due to differential dust loading in the atmosphere. Furthermore, surface wind can reshuffle the dust at the ground, leading to a local variability of albedo.

An alternative scenario, more likely to occur in the cryptic region (Piqueux et al., 2003; Kieffer et al., 2006; Langevin et al., 2006), implies CO_2 geysers ejecting dust at the surface of the ice. Piqueux et al., 2003 suggests that this process is in the origin of the asymmetry in albedo at global scale.

5.5 Cleaning process

Some authors found a correlation between albedo and insolation (Paige and Ingersoll, 1985; Kieffer et al., 2000) and claim that a cleaning process, controlled by insolation, progressively free the ice from its dust. Different processes can occur depending on particle size : dust can burrow through the ice or be ejected in the atmosphere (Kieffer et al., 2000; Portyankina and Markiewicz, 2003). Such mechanisms increase the albedo by decreasing the dust content within the ice deposit.

However these mechanisms alone cannot explain neither the asymmetry nor the local variability of albedo. Both cryptic and anti-cryptic sectors should be cleaned with the same intensity if the initial dust load is identical (fig 4). At local scale, the snowdrop time and the radiation budget distribution, that would sign the magnitude of the cleaning process, are not correlated (fig 8 and 9).

However, differences of dust load/size/shape distribution at the top of the CO_2 ice layer associated with the cleaning process can be a clue to explain the variability of albedo. Nevertheless, there is a negative feedback between albedo and cleaning: lower albedo, induces more solar energy absorbed, induces stronger cleaning, induces higher albedo. Such a mechanism tends to smooth differences in albedo.

5.6 Mechanical ablation

A process of mechanical ablation of the ice deposits, caused by atmosphere turbulence, would decrease the ice thickness and the albedo. In this scenario, suggested on Earth for the blue ice area in Antarctica (Bintanja, 1999), turbulence is linked with wind and surface roughness. Due to the low density of the atmosphere, this effect is likely for planet Mars only on small particles. Thomas et al., 1979 have interpreted that some frost streaks have an wind origin.

A Scales of interests

bin : element of a grid of the planetary surface determined in longitude and latitude. The sampling is 10° in longitude (from 0°E to 360°E) and 0.3° in latitude (from 53°S to 90°S).

meridian profile : profile of bins along a meridian (constant longitude), spanning 10° in longitude. From 53°S to 90°S for the model, from 30°S to 90°S for OMEGA observations.

bins of longitude and area are at a lower resolution than following objects :

facet : pixel in MOLA data that is used for the calculation of the insolation modulated by roughness. Spatial resolution is 920m in a south polar stereographic projection.

pixel : pixel in OMEGA observations, the spatial resolution can vary from 2 km to 700 m.

B Integration of insolation

Unfortunately the mathematical function Q can be negative with L. To force the integration on the positive part only (when the facet is illuminated), the absorbed energy Q is multiplied with a door function Π defined as following :

$$\Pi_{L_{min}}^{L_{max}}(L) = \begin{cases} 1, \; for \; L_{min} < L < L_{max} \\ 0, \; otherwise \end{cases} \tag{1}$$

$$\overrightarrow{r_{surf}} \bullet \overrightarrow{r_{sun}} = \sin(\phi)\sin(\delta) + \cos(\phi)\cos(\delta)\cos(L - \alpha) \tag{2}$$

$$\overrightarrow{n_{surf}} \bullet \overrightarrow{r_{sun}} = \sin(\phi_n)\sin(\delta) + \cos(\phi_n)\cos(\delta)\cos(L_n - \alpha) \tag{3}$$

With the following relations :
N/S slopes along meridian :

$$\phi_n = \begin{cases} \pi - \phi - \phi',\ for\ \phi + \phi' > \frac{\pi}{2} \\ -\pi - \phi - \phi',\ for\ \phi + \phi' < -\frac{\pi}{2} \\ \phi + \phi',\ otherwise \end{cases} \tag{4}$$

W/E slopes along parallel :

$$L_n = L + L' + L_c \begin{cases} L_c = 2\pi,\ for\ L + L' < 0 \\ L_c = -2\pi,\ for\ L + L' > 2\pi \\ L_c = 0,\ otherwise \end{cases} \tag{5}$$

Using those relations :

$$\phi' = \arctan(-\frac{\partial topo}{\partial \phi}) \tag{6}$$

$$L' = \arctan(-\frac{\partial topo}{\partial L}) \tag{7}$$

We assume that insolation is null when the sun is in the opposite side of the facet. This condition corresponds to a virtual displacement of the considered surface point from its real longitude L to L_n.
Our assumption can be written :

$$\overrightarrow{n_{surf}} \bullet \overrightarrow{r_{sun}} \geq 0 \Leftrightarrow \cos(L_n - \alpha) \geq -\tan(\phi_n) tan(\delta) \tag{8}$$

There are 3 different solutions for the equations depending on latitude and slopes :

(1) The sun never rises :

$$\overrightarrow{n}_{surf} \bullet \overrightarrow{r_{sun}} < 0 \Leftrightarrow 1 < -\tan(\phi_n)\tan(\delta) \tag{9}$$

$$W = \frac{1}{2\pi} \int_0^{2\pi} Q_{sun}\Pi_0^0 + Q_{scat}\Pi_0^0 + Q_{IR}\Pi_0^0 + Q_{floor}\Pi_0^{2\pi} dL \tag{10}$$

(2) The sun never sets :

$$\overrightarrow{n}_{surf} \bullet \overrightarrow{r_{sun}} > 0 \Leftrightarrow -1 > -\tan(\phi_n)\tan(\delta) \tag{11}$$

$$W = \frac{1}{2\pi}\int_0^{2\pi} Q_{sun}\Pi_0^{2\pi} + Q_{scat}\Pi_0^{2\pi} + Q_{IR}\Pi_0^{2\pi} + Q_{floor}\Pi_0^{2\pi} dL \tag{12}$$

(3) There is a sunrise and a sunset on the facet :

$$\overrightarrow{n_{surf}} \bullet \overrightarrow{r_{sun}} > 0 \Leftrightarrow -1 \leq -\tan(\phi_n)\tan(\delta) \leq +1 \tag{13}$$

We can define H_{n0} the local horary angle on the facet :

$$\cos(H_{n0}) = -\tan(\phi_n)\tan(\delta) \tag{14}$$

In that case, the sun illuminates the facet only when :

$$\overrightarrow{n_{surf}} \bullet \overrightarrow{r_{sun}} > 0 \Leftrightarrow \alpha - H_{n0} < L_n < \alpha + H_{n0} \tag{15}$$

Using equation 5, the condition on L is :

$$L_{min} = \alpha - H_{n0} - L' - L_c < L < \alpha + H_{n0} - L' - L_c = L_{max} \tag{16}$$

$$W = \frac{1}{2\pi}\int_0^{2\pi} Q_{sun}\Pi_{L_{min}}^{L_{max}} + Q_{scat}\Pi_{L_{min}}^{L_{max}} + Q_{IR}\Pi_0^{2\pi} + Q_{floor}\Pi_0^{2\pi} dL \tag{17}$$

C Summary of the parameter values used for the surface radiation budget

Parameters of the model, unit are noted in braket [], [1] denotes the absence of unit.

$R = 3,386,200$ [m] : radius of the planet

(x, y) [m] : map coordinates

(L,ϕ) [radian] : longitude (from 0 to 2π), latitude (from $-\frac{\pi}{2}$ to $\frac{\pi}{2}$)

γ [1] : local slope

Q_{sun} [W.m^{-2}] : instantaneous absorbed energy from the direct sunlight

Q_{scat} [W.m^{-2}] : instantaneous absorbed energy from the sunlight scattered by the atmosphere

Q_{IR} [W.m^{-2}] : instantaneous absorbed energy from the thermal emission by the atmosphere

Q_{floor} [W.m^{-2}] : instantaneous absorbed energy from the thermal emission by the neighboring facets

$\overrightarrow{r_{surf}}(L, \phi)$ [1]: normalized radius vector of a point at the surface assuming a spherical planet

$\overrightarrow{r_{sun}}(\alpha, \delta)$ [1]: normalized radius vector of the sub-solar point

$\overrightarrow{n_{surf}}(L_n, \phi_n)$ [1] : normalized vector of the direction normal to the local surface

$\Pi_{L_{min}}^{L_{max}}(L)$: door function.

$S_{sun} = 589$ [W.m^{-2}] : solar constant at the mean distance between Mars and the Sun $\langle d_{sun} \rangle$

r_{sun} [m] : Ratio of mean distance between Mars and the Sun over the distance at time t $\langle d_{sun} \rangle / d_{sun}(t)$. We calculate this distance $d_{sun}(t)$ for any date t using the astronomical parameters determined by the celestial measurements of Pathfinder at J2000 by Allison and McEwen (2000).

A_{vis} [1] : bolometric albedo in the visible. We assume a lambertian surface: $A_{dh,vis}(\theta_i) = A_{vis}$, no dependence on the incidence angle (see equation 1).

A_{IR} [1] : bolometric albedo in the thermal infra-red . We assume a lambertian surface : $A_{dh,IR}(\theta_i) = A_{IR}$, no dependence on the incidence angle. Albedo in the IR is linked to emissivity through $A_{IR} = 1 - \varepsilon$ (Warren et al., 1990).

$f = 0.06$: fraction of light absorbed by the atmosphere. This value was used in the modeling by Kieffer et al., 1977; Aharonson and Schorghofer, 2006. $f \simeq f_{scat} + f_{IR}$

$f_{scat} = 0.02$ [1] : fraction of the direct sunlight scattered by the atmosphere. This value was already used in the modeling by Kieffer et al., 1977; Aharonson and Schorghofer, 2006.

$f_{IR} = 0.04$ [1] : equivalent fraction of noon time direct sunlight scattered by the atmosphere. This value discussed by Haberle and Jakosky, 1991 was already used in the modeling by Aharonson and Schorghofer, 2006.

$H = 0.8$ [1] : Hurst exponent, describing the topographical roughness

ε [1] : thermal emissivity (see A_{IR})

$\sigma = 5.67 * 10^{-8}$ [W.m^{-2}.K^{-4}] : Stefan Boltzmann constant

T [K] : temperature of the surrounding soil. This temperature is assumed to be the same that for the considered facet. If the current facet is frosted whereas the surrounding ones are defrosted, Q_{floor} is underestimated.

D Summary of the parameters used for modeling the defrost mass balance

In addition to the radiative parameters described in section C we have :

$L_{CO_2} = 590 * 10^3$ [J.kg^{-1}] : latent heat for CO_2 sublimation

T_{surf} [K] : temperature of the facet

M_{CO_2} [kg.m^{-2}] : CO_2 mass of the frost layer

t [s] : time

Acknowledgements

This work is supported by a PhD grant from the 'Ministère délégué à l'Enseignement supérieur et à la Recherche' and by a contract with CNES through its 'Système Solaire' program. We thank the OMEGA team at IAS for support with sequencing and data download activities. The authors would like to thank Nicolas Jourdain for useful discussions.

References

Aharonson, O., Mar. 2004. Sublimation at the Base of a Seasonal CO_2 Slab on Mars. In: Mackwell, S., Stansbery, E. (Eds.), Lunar and Planetary Institute Conference Abstracts. pp. 1918–+.

Aharonson, O., Schorghofer, N., Nov. 2006. Subsurface ice on Mars with rough topography. Journal of Geophysical Research (Planets) 111, 11007–+.

Aharonson, O., Zuber, M. T., Rothman, D. H., Oct. 2001. Statistics of Mars' topography from the Mars Orbiter Laser Altimeter: Slopes, correlations, and physical models. Journal of Geophysical Research 106, 23723–23736.

Aharonson, O., Zuber, M. T., Smith, D. E., Neumann, G. A., Feldman, W. C., Prettyman, T. H., May 2004. Depth, distribution, and density of CO_2 deposition on Mars. Journal of Geophysical Research (Planets) 109, 5004–+.

Allison, M., McEwen, M., Feb. 2000. A post-Pathfinder evaluation of areocentric solar coordinates with improved timing recipes for Mars seasonal/diurnal climate studies. Planetary and Space Science 48, 215–235.

Bintanja, R., 1999. On the glaciological, meteorological, and climatological significance of antarctic blue ice areas. Reviews of Geophysics 37, 337–360.

Brown, G. N. J., Ziegler, W. T., 1979. Vapor pressure and heats of vaporization and sublimation of liquids and solids of interest in cryogenics below 1-atm pressure. Advences in Cryogenic Engineering 25, 662–670.

Campbell, B. A., Ghent, R. R., Shepard, M. K., Feb. 2003. Limits on inference of Mars small-scale topography from MOLA data. Geophysical Research Letters 30, 15–1.

Campbell, W. W., Jan. 1895. The Irregular Waning of the South Polar CAP of Mars. Publications of the Astronomical Society of the Pacific 7, 40–+.

Colaprete, A., Barnes, J. R., Haberle, R. M., Hollingsworth, J. L., Kieffer, H. H., Titus, T. N., May 2005. Albedo of the south pole on Mars determined by topographic forcing of atmosphere dynamics. Nature 435, 184–188.

Colaprete, A., Toon, O. B., Jul. 2002. Carbon dioxide snow storms during the polar night on Mars. Journal of Geophysical Research (Planets) 107, 5–1.

Eluszkiewicz, J., May 1993. On the microphysical state of the martian seasonal caps. Icarus 103 (1), 43–48.
URL http://www.sciencedirect.com/science/article/B6WGF-45PTGGM-6T/2/17eaeb1d224a

Eluszkiewicz, J., Moncet, J.-L., Dec. 2003. A coupled microphysical/radiative transfer model of albedo and emissivity of planetary surfaces covered by volatile ices. Icarus 166 (2), 375–384.
URL http://www.sciencedirect.com/science/article/B6WGF-49V1DPH-3/2/12ed8d86bc224

Forget, F., 1998. Mars CO_2 ice polar caps. In: Schmitt, B., de Bergh, C., Festou, M. (Eds.), Solar System Ices. Vol. 227 of Astrophysics and Space Science Library. Kluwer, pp. 477–507.

Forget, F., Hourdin, F., Fournier, R., Hourdin, C., Talagrand, O., Collins, M., Lewis, S. R., Read, P. L., Huot, J.-P., Oct. 1999. Improved general circulation models of the Martian atmosphere from the surface to above 80 km. Journal of Geophysical Research 104, 24155–24176.

Forget, F., Hourdin, F., Talagrand, O., Feb. 1998. CO_2 Snowfall on Mars: Simulation with a General Circulation Model. Icarus 131, 302–316.

Haberle, R. M., Jakosky, B. M., Apr. 1991. Atmospheric effects on the remote determination of thermal inertia on Mars. Icarus 90, 187–204.

Hapke, B., 1993. Theory of reflectance and emittance spectroscopy. Topics in Remote Sensing, Cambridge, UK: Cambridge University Press.

James, P. B., Briggs, G., Barnes, J., Spruck, A., Jun. 1979. Seasonal recession of Mars' south polar CAP as seen by Viking. Journal of Geophysical Research 84, 2889–2922.

Kelly, N. J., Boynton, W. V., Kerry, K., Hamara, D., Janes, D., Reedy, R. C., Kim, K. J., Haberle, R. M., Dec. 2006. Seasonal polar carbon dioxide frost on Mars: CO_2 mass and columnar thickness distribution. Journal of Geophysical Research (Planets) 111, 3–+.

Kieffer, H. H., Christensen, P. R., Titus, T. N., Aug. 2006. Co2 jets formed by sublimation beneath translucent slab ice in mars' seasonal south polar ice cap. Nature 442 (7104), 793–796.
URL http://dx.doi.org/10.1038/nature04945

Kieffer, H. H., Martin, T. Z., Peterfreund, A. R., Jakosky, B. M., Miner, E. D., Palluconi, F. D., Sep. 1977. Thermal and albedo mapping of Mars during the Viking primary mission. Journal of Geophysical Research 82, 4249–4291.

Kieffer, H. H., Titus, T. N., Mullins, K. F., Christensen, P. R., Apr. 2000. Mars south polar spring and summer behavior observed by TES: Seasonal cap evolution controlled by frost grain size. Journal of Geophysical Research 105, 9653–9700.

Langevin, Y., Douté, S., Vincendon, M., Poulet, F., Bibring, J.-P., Gondet, B., Schmitt, B., Forget, F., Aug. 2006. No signature of clear co2 ice from the 'cryptic' regions in mars' south seasonal polar cap. Nature 442 (7104), 790–792.
URL http://dx.doi.org/10.1038/nature05012

Langevin, Y., Montmessin, F., Forget, F., Vincendon, M., Douté, S., Poulet, F., Bibring, J.-P., Gondet, B., 2007. Observations of the south seasonal cap of mars during retreat in 2004-2006 by the omega visible/nir imaging spectrometer on board mars express. JGR Planet, submited.

Laskar, J., Joutel, F., Boudin, F., Mar. 1993. Orbital, precessional, and insolation quantities for the Earth from -20 MYR to +10 MYR. Astronomy and Astrophysics 270, 522–533.

Leighton, R. R., Murray, B. C., Jul. 1966. Behavior of carbon dioxide and other volatiles on Mars. Science 153, 136–144.

Lewis, S. R., Collins, M., Read, P. L., Forget, F., Hourdin, F., Fournier, R., Hourdin, C., Talagrand, O., Huot, J.-P., Oct. 1999. A climate database for Mars. Journal of Geophysical Research 104, 24177–24194.

Litvak, M. L., Mitrofanov, I. G., Kozyrev, A. S., Sanin, A. B., Tretyakov, V. I., Boynton, W. V., Kelly, N. J., Hamara, D., Saunders, R. S., Feb. 2007. Long-term observations of southern winters on Mars: Estimations of column thickness, mass, and volume density of the seasonal CO_2 deposit from HEND/Odyssey data. Journal of Geophysical Research (Planets) 112, 3–+.

Malamud, B. D., Turcotte, D. L., Aug. 2001. Wavelet analyses of Mars polar topography. Journal of Geophysical Research 106, 17497–17504.

Murchie, S. L., Arvidson, R. E., Bedini, P., Beisser, K., Bibring, J.-P., Bishop, J., Boldt, J. D., Choo, T. H., Clancy, R. T., Darlington, E. H., Des Marais, D., Espiritu, R., Fasold, M. J., Fort, D., Green, R. N., Guinness, E., Hayes, J. R., Hash, C., Heffernan, K. J., Hemmler, J., Heyler, G. A., Humm, D. C., Hutchison, J., Izenberg, N. R., Lee, R. E., Lees, J. J., Lohr, D. A., Malaret, E. R., Martin, T., Morris, R. V., Mustard, J. F., Rhodes, E. A., Robinson, M. S., Roush, T. L., Schaefer, E. D., Seagrave, G. G., Silverglate, P. R., Slavney, S., Smith, M. F., Strohbehn, K., Taylor, H. W., Thompson, P. L., Tossman, B. E., Dec. 2004. CRISM (Compact Reconnaissance Imag-

ing Spectrometer for Mars) on MRO (Mars Reconnaissance Orbiter). In: Nardell, C. A., Lucey, P. G., Yee, J.-H., Garvin, J. B. (Eds.), Applications with Weather Satellites II. Edited by Menzel, W. Paul; Iwasaki, Toshiki. Proceedings of the SPIE, Volume 5660, pp. 66-77 (2004). pp. 66–77.

Paige, D. A., Ingersoll, A. P., Jun. 1985. Annual heat balance of Martian polar caps - Viking observations. Science 228, 1160–1168.

Piqueux, S., Byrne, S., Richardson, M. I., Aug. 2003. Sublimation of Mars's southern seasonal CO_2 ice cap and the formation of spiders. Journal of Geophysical Research (Planets) 108, 3–1.

Pollack, J. B., Haberle, R. M., Schaeffer, J., Lee, H., Feb. 1990. Simulations of the general circulation of the Martian atmosphere. I - Polar processes. Journal of Geophysical Research 95, 1447–1473.

Portyankina, G., Markiewicz, W. J., Oct. 2003. Model for Formation of Spider Patterns in the Cryptic Region. In: Clifford, S., Doran, P., Fisher, D., Herd, C. (Eds.), Third International Conference on Mars Polar Science and Exploration. pp. 8026–+.

Press, W. H., Flannery, B. P., Teukolsky, S. A., Vetterling, W. T., 1986-1992. Numerical Recipes in Fortran 77 : the art of scientific computing. Cambridge University Press, Ch. 4.4, pp. 110–114.

Putzig, N. E., Mellon, M. T., Kretke, K. A., Arvidson, R. E., Feb. 2005. Global thermal inertia and surface properties of Mars from the MGS mapping mission. Icarus 173, 325–341.

Sayles, R. S., Thomas, T. R., Feb. 1978. Surface topography as a nonstationary random process. Nature 271 (5644), 431–434.
URL http://dx.doi.org/10.1038/271431a0

Schmidt, F., Douté, S., Schmitt, B., 2007. Wavanglet: An efficient supervised classifier for hyperspectral images. Geoscience and Remote Sensing, IEEE Transactions on 45 (5), 1374–1385.

Schmitt, B., Schmidt, F., Douté, S., Langevin, Y., Forget, F., Bibring, J.-P., Gondet, B., Omega Team, Oct. 2006. Recession of the Northern Seasonal Condensates on Mars by OMEGA/Mars Express. LPI Contributions 1323, 8050–+.

Schorghofer, N., Aharonson, O., May 2005. Stability and exchange of subsurface ice on Mars. Journal of Geophysical Research (Planets) 110, 5003–+.

Shchuko, O. B., Kartashov, D. V., Picardi, G., Orosei, R., Jan. 2003. Martian underground water detection: Thermal model and simulations of radar signal propagation. Journal of Geophysical Research (Planets) 108, 3–1.

Shepard, M. K., Campbell, B. A., Aug. 1998. Shadows on a Planetary Surface and Implications for Photometric Roughness. Icarus 134, 279–291.

Shepard, M. K., Campbell, B. A., Bulmer, M. H., Farr, T. G., Gaddis, L. R., Plaut, J. J., Dec. 2001. The roughness of natural terrain: A planetary and remote sensing perspective. Journal of Geophysical Research 106, 32777–32796.

Thomas, P., Veverka, J., Campos-Marquetti, R., Aug. 1979. Frost streaks in the south polar CAP of Mars. Journal of Geophysical Research 84, 4621–

4633.

Veverka, J., Goguen, J., Dec. 1973. The Nonuniform Recession of the South Polar Cap of Mars. Journal of the Royal Astronomical Society of Canada 67, 273–+.

Warren, S. G., Wiscombe, W. J., Firestone, J. F., Aug. 1990. Spectral albedo and emissivity of CO2 in Martian polar caps - Model results. Journal of Geophysical Research 95, 14717–14741.